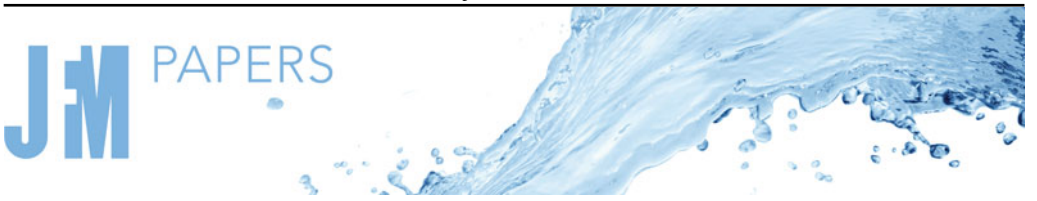
J. Fluid Mech. (2026), *vol.* 1037, A31, doi:10.1017/jfm.2026.11695



Dynamical evolution of buoyancy-driven flow induced by submerged thermal vertical pipes

Bingchuan Nie[1], **Mengfan Lu**[1] **and Feng Xu**[1]

[1]School of Physical Science and Engineering, Beijing Jiaotong University, Beijing 100044, PR China

Corresponding author: Bingchuan Nie, bcnie@bjtu.edu.cn

(Received 7 November 2025 UTC; revised 12 May 2026 UTC; accepted 14 May 2026 UTC)

The buoyancy-driven natural convection induced by submerged thermal vertical pipes acts as a passive thermal pump without moving parts, characterised by efficient heat transfer. It comprises three key components: natural convection inside the pipe, a thermal plume above the pipe exit and a radial intrusion flow along the upper free surface. Our previous work (Nie & Xu 2022 *J. Fluid Mech.*, vol. **937**, A29) investigated transient natural convection in a vertical pipe for fluids with a Prandtl number (Pr) less than unity. In this study we extend the scaling analysis to water ($Pr > 1$), which exhibits fundamentally different dynamics due to the dominance of viscous diffusion over thermal diffusion. We identify three distinct flow configurations, each undergoing a transient development before reaching a fully developed state: (i) the boundary layer flow; (ii) the bulk momentum flow with thermal boundary layer, characterised by a merged velocity layer but a distinct thermal layer; and (iii) the pipe flow resulting from the simultaneous merging of both the velocity and thermal boundary layers. Scaling laws governing the flow and heat transfer across these regimes are derived. Moreover, scaling analyses for the external thermal plume and the radial intrusion flow are also performed. All scaling laws are validated, for the axisymmetric and laminar regime, by extensive numerical simulations.

Key words: buoyant boundary layers, plumes/thermals, pipe flow boundary layer

1. Introduction

When a vertical open-ended pipe immersed in a fluid is heated, buoyancy forces arise from the change in fluid density. This drives internal convection within the pipe, characterised by cooler fluid being drawn into the bottom while a rising thermal plume emanates from the top exit. Upon impinging on an upper boundary (e.g. a free surface), this plume transitions into a radial intrusion along the boundary. This flow acts as a passive thermal pump without moving parts. It can leverage a chimney effect that, by suppressing

© The Author(s), 2026. Published by Cambridge University Press.

https://doi.org/10.1017/jfm.2026.11695 Published online by Cambridge University Press

lateral momentum exchange, enhances vertical mass flux and heat transfer, and exhibits a continuous topological transformation of streamlines from a vertical axisymmetric jet to a radial horizontal intrusion along the free surface. Understanding the dynamical evolution of this flow system is therefore of fundamental interest in fluid mechanics. Moreover, it can also provide critical physical insights for applications ranging from classical systems, such as open thermosyphons (Japikse 1973) and nuclear passive cooling systems (Ohk & Chung 2017), to emerging technologies, like single-phase immersion cooling for electronics (Huang *et al.* 2023) and artificial sea upwelling (Lovelock & Rapley 2007).

The central element of this flow, buoyancy-driven natural convection within the pipe, has been the subject of extensive research. Early investigations primarily addressed the fully developed stage, aiming to establish the relationship between the Nusselt number and the Rayleigh number (Davis & Perona 1971; Dyer 1975). Subsequent research has expanded to consider other key aspects, including the spatial development at the pipe inlet and outlet (Takhar 1968), and the influence of parameters like the pipe inclination angle (Al-Arabi, Khamis & Abd-Ul-Aziz 1991; Bae, Kim & Chung 2018).

Natural convection in pipes exhibits significant transient characteristics in response to system start-up, a common scenario in practical applications. The flow and heat transfer processes of transient natural convection on a vertical flat plate are well understood by the pioneering work of Patterson & Imberger (1980). Inspired by this approach, scaling analyses have also been successfully applied to study the effects of features like fins on flat walls (Xu, Patterson & Lei 2009), wedged water bodies (Mao, Lei & Patterson 2010; Yu, Patterson & Lei 2015) and the influence of key parameters such as the Prandtl number (Lin & Armfield 2012). However, the applicability of flat-plate findings to pipes is limited by the effects of wall curvature. These are frequently neglected for large radii (Lin & Armfield 2001), but in contrast, they become significant and a source of considerable error for pipes with a small radii of curvature.

Research on curvature effects in natural convection has evolved along two main paths. The first path examines convex curvatures, which correspond to flow on the exterior of cylinders, as explored in studies such as Cebeci, Wogulis & Partin (1968), Goodrich & Marcum (2019), Dash & Dash (2020), Zhao, Lei & Patterson (2021), Liu & Liu (2022). For such external flows, it has been found that when the radius of curvature is comparable to the boundary layer thickness, the curvature effect can significantly alter the diffusion term, enhancing heat transfer and also modifying the flow transition, and being comparable in magnitude to the leading-order physics. Scaling laws for the flow and heat transfer in this type of natural convection were provided by Zhao *et al.* (2021) and Liu & Liu (2022).

The second path addresses concave curvatures, exemplified by flow inside cylindrical pipes. In contrast to external flows, curvature inside pipes goes beyond quantitative modifications to alter the very nature of the flow (Pécheux *et al.* 1994; Ohk & Chung 2017), but can even lead to a duct flow regime in which the thermal boundary layer merges at the pipe axis (Nie & Xu 2022), a regime that does not exist for flow over flat plates or the outside of cylinders. Furthermore, the boundary layer regime and the duct flow regime within the pipe differ fundamentally, leading to distinct heat transfer and flow behaviours. For the constant heat flux case, for instance, the flow rate scaling can transition from $Ra_q^{1/5}$ for the boundary layer regime to $Ra_q^{1/2}$ for the duct flow regime, while the influence of the slenderness ratio also undergoes a fundamental change between these two regimes (see table 1 of Nie & Xu 2022). Here, Ra_q is the Rayleigh number based on heat flux. There is also work on vertical eccentric annuli, where both convex and concave curvatures are present (Mokheimer & El-Shaarawi 2007; Hosseini *et al.* 2012). Related studies have

https://doi.org/10.1017/jfm.2026.11695 Published online by Cambridge University Press

primarily been experimental or numerical, with theoretical analysis remaining challenging and largely unexplored.

The literature most directly relevant to the present problem is our previous work (Nie & Xu 2022). In that paper, we classified the regimes for transient natural convection in a pipe into boundary layer flow and duct flow regimes (characterised by thermal boundary layer merging), and provided scaling laws for quantities such as flow rate with the Rayleigh number and curvature effects. However, the analysis in that study was limited to $Pr < 1$ fluids, in which the thermal and velocity boundary layers grow at comparable rates, leading to their simultaneous merging at the pipe centre. In the scenario of $Pr > 1$, the velocity boundary layer becomes much thicker than the thermal boundary layer. Consequently, three distinct scenarios can arise within the pipe: non-merged boundary layers, a merged velocity boundary layer with a non-merged thermal boundary layer and the simultaneous merging of both boundary layers. The combination of these three scenarios with the flow evolution through start-up, transitional and fully developed stages results in a more complex regime map. The scaling laws relating flow and heat transfer in these regimes to the governing parameters like the Rayleigh number and slenderness ratio have not yet been established.

Furthermore, the natural convection within the pipe also influences the behaviour of the external thermal plume and the spreading flow along the free surface. Classical plume models, such as the Morton–Taylor–Turner model (Morton, Taylor & Turner 1956) and its extensions (Hunt & Van den Bremer 2011), have been successfully applied to fully developed plumes. Separately, exact similarity solutions exist for axisymmetric heated jets (Brand & Lahey 1967). However, these models rely on self-similarity assumptions that are typically valid only at some distance from the source, and the volume, momentum and buoyancy fluxes must be predetermined. These fluxes, in turn, are highly dependent on the geometry and thermal characteristics of the heat source. The influence of source geometry on plume development has been recognised in a few contexts. Studies on laminar starting plumes generated by an electrical coil show that the flow undergoes an acceleration stage within approximately five times the heater size before reaching a steady ascent velocity (Kaminski & Jaupart 2003). Scaling relations for plume characteristics have also been examined for other specific geometries, such as a horizontal plate (Jiang *et al.* 2021) and a top-open cylinder heated from below (Zhang, Nie & Xu 2023). For the specific configuration in this study, a direct link between the downstream plume dynamics and the parameters governing natural convection inside a heated vertical pipe has not yet been established. Therefore, deriving scaling laws that capture the dependence of the external thermal plume and its radial intrusion on the natural convection inside the pipe is a natural extension worth exploring.

This paper focuses on transient natural convection inside a vertical pipe heated with constant heat flux submerged in a water body. It identifies the different existing regimes and provides scaling laws for each regime relating key quantities, including the characteristic thickness and temperature of the thermal boundary layer and the characteristic thickness, velocity and flow rate of the velocity boundary layer, to the slenderness ratio and Rayleigh number. Furthermore, scaling analyses are conducted for the rising thermal plume and free surface spreading flow pipe flow resulting from the simultaneous merging of both the velocity and thermal boundary layers. Finally, the theoretical scaling laws are validated against numerical simulation results. The rest of this paper is organised as follows: § 2 describes the physical problem; scaling analysis for the natural convection in the pipe, thermal plume outside the pipe and radial intrusion flow near the free surface is presented in §§ 3, 4 and 5, respectively. Section 6 presents the validation of the scaling laws by the numerical results. Section 7 concludes the paper.

https://doi.org/10.1017/jfm.2026.11695 Published online by Cambridge University Press

2. Problem description

The physical model we considered is a circular vertical pipe submerged in water. When the pipe is heated with a spatially uniform and temporally constant heat flux, heat transfer and buoyancy-driven flow arise. The flow system consists of flow in the pipe, thermal plume above the pipe and intrusion flow along the upper free surface, as sketched in figure 1. The Boussinesq approximation is invoked as the flow is driven by buoyancy with only small relative density variations, and the Soret and Dufour effects are neglected as higher-order phenomena. Under the assumption of axisymmetry, the conservation equations of mass, momentum and energy expressed in a cylindrical coordinate system read

$$\frac{1}{r}\frac{\partial(ru_r)}{\partial r}+\frac{\partial u_z}{\partial z}=0, \tag{2.1}$$

$$\frac{\partial u_r}{\partial t}+u_r\frac{\partial u_r}{\partial r}+u_z\frac{\partial u_r}{\partial z}=-\frac{1}{\rho}\frac{\partial p}{\partial r}+\nu\left[\frac{1}{r}\frac{\partial}{\partial r}\left(r\frac{\partial u_r}{\partial r}\right)-\frac{u_r}{r^2}+\frac{\partial^2 u_r}{\partial z^2}\right], \tag{2.2}$$

$$\frac{\partial u_z}{\partial t}+u_r\frac{\partial u_z}{\partial r}+u_z\frac{\partial u_z}{\partial z}=-\frac{1}{\rho}\frac{\partial p}{\partial z}+\nu\left[\frac{1}{r}\frac{\partial}{\partial r}\left(r\frac{\partial u_z}{\partial r}\right)+\frac{\partial^2 u_z}{\partial z^2}\right]+g\beta(T-T_0), \tag{2.3}$$

$$\frac{\partial T}{\partial t}+u_r\frac{\partial T}{\partial r}+u_z\frac{\partial T}{\partial z}=\kappa\left[\frac{1}{r}\frac{\partial}{\partial r}\left(r\frac{\partial T}{\partial r}\right)+\frac{\partial^2 T}{\partial z^2}\right]. \tag{2.4}$$

Here r and z are the dimensional cylindrical coordinates as sketched in figure 1, and t is time; u_r and u_z are corresponding velocity components; T and p are the temperature and pressure, respectively; ν, κ, β and g are the kinematic viscosity, diffusivity, thermal expansion coefficient and gravity acceleration, respectively.

The fluid in the pipe is initially at a uniform temperature and motionless. The initial conditions are expressed as

$$u_r(r,z,0)=u_z(r,z,0)=0 \tag{2.5}$$

and

$$T(r,z,0)=T_0. \tag{2.6}$$

The pipe wall is assumed to be non-slip, which gives

$$u_r(R,z,t)=u_z(R,z,t)=0. \tag{2.7}$$

Here, R is the radius of the pipe. The constant heat flux boundary condition is imposed on the wall of the pipe and reads

$$\lambda\partial T(R,\phi,z,t)/\partial r=q. \tag{2.8}$$

Here λ is the fluid conductivity, q is the heat flux through the wall, which is uniform and constant, and ϕ denotes the azimuthal angle in the cylindrical coordinate system.

As the impinging thermal plume has a small Froude number ($Fr\lesssim 1$) and can hardly cause significant deformation of the free surface, the rigid and stress-free boundary condition,

$$\partial u_r/\partial r=0,\ u_z=0, \tag{2.9}$$

is imposed on the free surface $z=L+H$.

The heat transfer and flow are determined by the Rayleigh number (Ra_q), Prandtl number (Pr) and the ratio of the slenderness ratio of the pipe (S) and the non-dimensional

https://doi.org/10.1017/jfm.2026.11695 Published online by Cambridge University Press

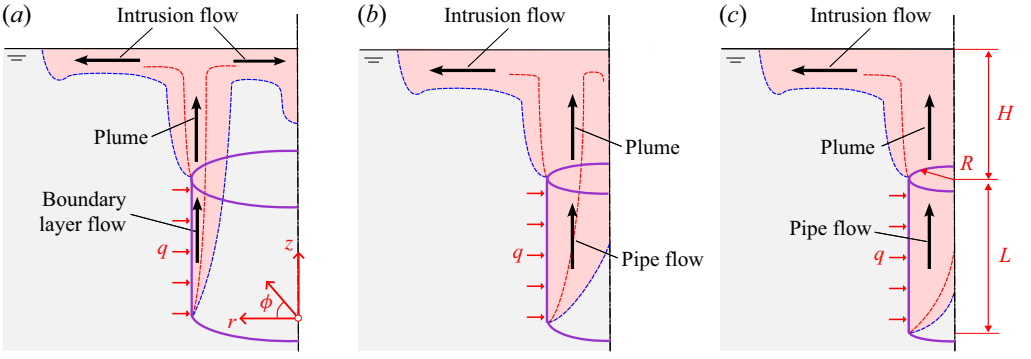


Figure 1. Three different scenarios of thermal and velocity boundary layers. Here Pr is larger than unity. The red and blue dash lines correspond to the boundary of thermal and velocity boundary layers, respectively. (*a*) Type I: boundary layer flow. (*b*) Type II: bulk momentum with thermal boundary layer flow. (*c*) Type III: pipe flow.

submerged depth (D). The working fluid in this study is water with a Prandtl number $Pr = 7.0$ corresponding to 293 K. This means that the system is governed by

$$Ra_q = \frac{g\beta q L^4}{\lambda \kappa \nu}, \qquad S = \frac{L}{R}, \qquad D = \frac{H}{R}. \tag{2.10}$$

3. Flow in the pipe

The flow in the pipe is driven by buoyancy, which is generated by heat flux through the pipe wall. As the Prandtl number of water is greater than unity, momentum diffuses more rapidly than heat, resulting in a velocity boundary layer that is always thicker than the thermal boundary layer. Consequently, three distinct scenarios of heat and mass transfer, designated as boundary layer flow (type I), bulk momentum with thermal boundary layer flow (type II) and pipe flow (type III), may exist, as illustrated in figure 1. In type I boundary layer flow, both the thickness of the velocity boundary layer and thermal boundary layer are thinner than R, in which heat and mass transfer are localised within the boundary region adjacent to the wall. Type II is characterised by a velocity boundary layer that merges at the centreline, while the thermal boundary layer remains distinct. This configuration, illustrated in figure 2(*a*), leads to global mass transfer but localised heat transfer. Once the velocity boundary layer merges at the centreline, the stack (chimney) effect becomes fully established, resulting in a constant flow rate at any cross-section along the pipe. Type III pipe flow occurs when both the velocity and thermal boundary layers merge at the centreline, as shown in figure 2(*b*), in which both heat and mass transfer become global throughout the pipe cross-section.

The transient heat transfer and flow in the pipe will experience an unsteady stage followed by a fully developed stage. With the three scenarios in figure 1, there will be at least three different routes of development as summarised in figure 3. Route R1: unsteady type I → fully developed type I; route R2: unsteady type I → unsteady type II → fully developed type II; route R3: unsteady type I → unsteady type II → unsteady type III → fully developed type III. The key quantities including the thickness of the thermal and velocity boundary layers, typical velocity, flow rate and temperature at the outlet of the pipe are discussed for each route in this section.

https://doi.org/10.1017/jfm.2026.11695 Published online by Cambridge University Press

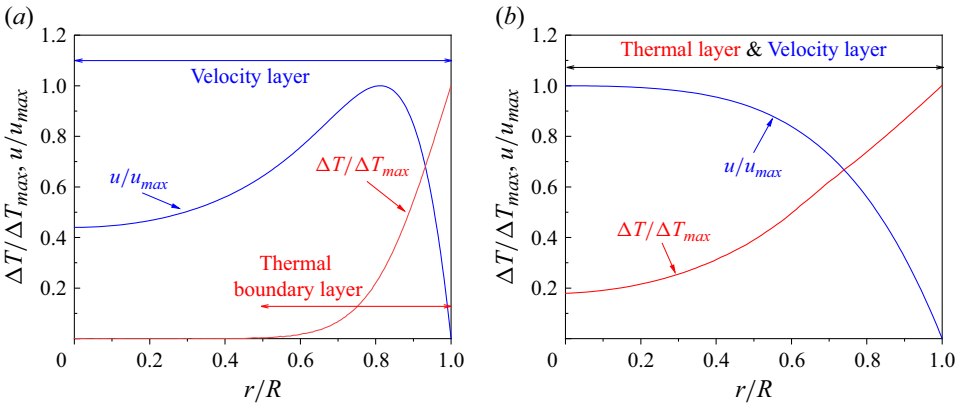


Figure 2. Typical fully developed temperature and velocity profiles in the pipe. The profiles shown are the numerical results of cases (*a*) $Ra_q = 10^6$, $S = 2.0$ and $D = 1.33$; (*b*) $Ra_q = 10^6$, $S = 6.0$ and $D = 4.00$ at $z = 0.75L$. They correspond to types II and III, respectively.

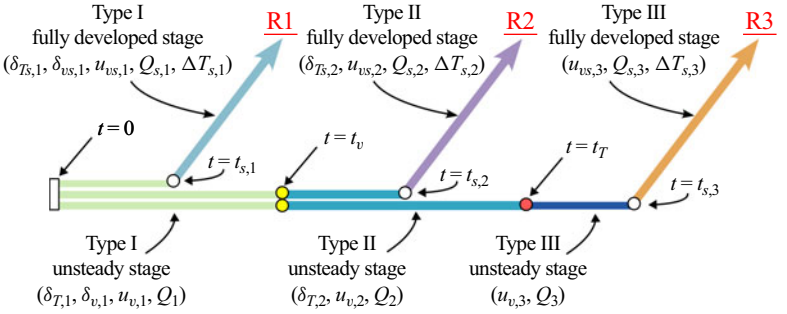


Figure 3. Three routes of the heat transfer and flow in the pipes R1, R2 and R3. Here δ, u, Q and ΔT represent the typical thickness of the boundary layer, velocity, flow rate and temperature difference. The subscripts T and v represent the thermal and velocity boundary layers, respectively; 1, 2 and 3 correspond to types I, II and III in figure 1, respectively; s represents the fully developed stage.

3.1. *Route R1*

Once the isoflux boundary condition is imposed on the pipe, a thermal boundary layer forms adjacent to the inner surface of the pipe. When t is small at the very early stage, the flow is weak so that the heat transfer by convection is neglected. The energy equation (2.4) can be simplified as the balance of unsteady and conduction terms, which is written in the integration form as (Nie & Xu 2022)

$$\int_{R-\delta_{T,1}}^{R} \frac{\partial T}{\partial t} r \mathrm{d}r \sim \int_{R-\delta_{T,1}}^{R} \kappa \frac{\partial}{\partial r}\left(r \frac{\partial T}{\partial r}\right) \mathrm{d}r. \tag{3.1}$$

The left-hand side term can be estimated by $\Delta T(R^2 - (R-\delta_{T,1})^2)/(2t)$ and the right-hand side term by $\kappa R \Delta T/\delta_{T,1}$. We obtain a relation of $\delta_{T,1}$ as

$$\delta_{T,1} \sim \kappa^{1/2} t^{1/2} \cdot \left(1 + \frac{\delta_{T,1}^3}{2\kappa t R}\right)^{1/2} \sim \kappa^{1/2} t^{1/2} \eta_{T,1}, \tag{3.2}$$

where $\kappa^{1/2} t^{1/2}$ is the thickness of the thermal boundary layer on a flat wall (Lin & Armfield 2013; Ma *et al.* 2018*a*). Hence, $\eta_{T,1}$ represents the non-dimensional curvature

https://doi.org/10.1017/jfm.2026.11695 Published online by Cambridge University Press

effect on $\delta_{T,1}$, which is always larger than unity. Here $\eta_{T,1}$ increases with $\delta_{T,1}$, implying that the curvature effect becomes increasingly prominent with the increase of $\delta_{T,1}$.

When the buoyancy-driven convection becomes non-negligible, a two-layer structure can be observed, which is a thermal boundary layer and a velocity boundary layer. As the Prandtl number of water is larger than unity, the thickness of the velocity boundary layer is always larger than that of the thermal boundary layer. It is noteworthy that the velocity boundary layer has also been divided into an inner and an outer viscous layer in the study of transient natural convection adjacent to a flat wall (Lin *et al.* 2009). Instead of the three-layer model in Lin *et al.* (2009), we follow the two-layer model as in Patterson & Imberger (1980) for the sake of simplicity of the scaling laws.

In the thermal boundary layer where $\delta_{T,1} < r < R$, (2.3) can be simplified as the balance between the viscous and buoyancy terms, as the inertial term is much smaller than the viscous term for $Pr > 1$ (Patterson & Imberger 1980), i.e.

$$-\nu \int_{R-\delta_{T,1}}^{R} \frac{\partial}{\partial r}\left(r\frac{\partial u_z}{\partial r}\right) \mathrm{d}r \sim \int_{R-\delta_{T,1}}^{R} g\beta\Delta T r \mathrm{d}r. \tag{3.3}$$

The left-hand side term may be estimated by $\nu u_{v,1} R/\delta_{T,1} + \nu u_{v,1}(R-\delta_{T,1})/(\delta_{v,1} - \delta_{T,1})$, where $u_{v,1}$ is the typical velocity of the velocity boundary layer. The right-hand side term by $g\beta q\delta_{T,1}(R^2 - (R-\delta_{T,1})^2)/(2\lambda)$ considering $q \sim \lambda\Delta T/\delta_{T,1}$. Using (3.2) and considering that $\delta_{v,1}$ is much larger than $\delta_{T,1}$ for water, (3.3) gives a scaling law of the velocity as

$$u_{v,1} \sim \frac{Ra_q}{S^4}\frac{\kappa^2 t}{R^3} \cdot \frac{1-\delta_{T,1}/\delta_{v,1}}{(\delta_{T,1}/R)^{-1} - \delta_{T,1}/\delta_{v,1}} \sim \frac{Ra_q}{S^4}\frac{\kappa^2 t}{R^3}\frac{\delta_{T,1}}{R} \sim \frac{Ra_q}{S^4}\frac{\kappa^{5/2}t^{3/2}}{R^4}\eta_{T,1}. \tag{3.4}$$

Notably, for natural convection adjacent to a flat vertical wall, the typical vertical velocity scales as t under isothermal conditions (Patterson & Imberger 1980) and as $t^{3/2}$ under isoflux conditions (Lin & Armfield 2013). Equation (3.4) shows that the curvature effect on the velocity is captured by $\eta_{T,1}$, similarly to its effect on $\delta_{T,1}$.

In the layer $\delta_{T,1} < r < \delta_{v,1}$, the dominant balance in the momentum equation (2.3) is between the viscous and inertial terms, which can be written as

$$\int_{R-\delta_{v,1}}^{R-\delta_{T,1}} r\frac{\partial u_z}{\partial t}\mathrm{d}r \sim \nu \int_{R-\delta_{v,1}}^{R-\delta_{T,1}} \frac{\partial}{\partial r}(r\frac{\partial u_z}{\partial r})\mathrm{d}r. \tag{3.5}$$

The left-hand side term can be estimated by $u_{v,1}((R-\delta_{T,1})^2 - (R-\delta_{v,1})^2)/(2t)$ and the right-hand side term by $\nu(R-\delta_{T,1})u_{v,1}/(\delta_{v,1}-\delta_{T,1})$ as $\partial u_z/\partial r = 0$ at $r = R-\delta_{v,1}$. We can obtain

$$\delta_{v,1} \sim \nu^{1/2}t^{1/2}\left[\frac{\delta_{T,1}}{\nu^{1/2}t^{1/2}} + \left(\frac{R-\delta_{T,1}}{2R-\delta_{T,1}-\delta_{v,1}}\right)^{1/2}\right] \sim \nu^{1/2}t^{1/2}\eta_{v,1}. \tag{3.6}$$

Here, $\nu^{1/2}t^{1/2}$ is the thickness of the velocity boundary layer for natural convection adjacent to a flat vertical wall, as obtained previously (Patterson & Imberger 1980); $\eta_{v,1}$ represents the non-dimensional curvature effect on the thickness of the velocity boundary layer.

Additionally, the flow rate $Q_{o,1}$ at the outlet of the pipe can be estimated by $2\pi R\delta_{v,1}u_{v,1}$, which reads

$$Q_{o,1} \sim \frac{Ra_q}{S^4} \cdot \frac{\kappa^3 t^2}{R^3}\eta_{T,1}\eta_{v,1}. \tag{3.7}$$

https://doi.org/10.1017/jfm.2026.11695 Published online by Cambridge University Press

The subscript o represents quantities measured at the outlet of the pipe hereafter.

With the increase of the flow rate, the heat convected away increases and balances that conducted in, and the flow and heat transfer become fully developed. The balance between the advection and diffusion terms in the energy equation (2.4) gives

$$\int_{R-\delta_{Ts,1}}^{R} u_z \frac{\partial T}{\partial z} r \mathrm{d}r \sim \int_{R-\delta_{Ts,1}}^{R} \kappa \frac{\partial}{\partial r}\left(r \frac{\partial T}{\partial r}\right) \mathrm{d}r. \tag{3.8}$$

The left-hand side term can be estimated by $u_{vs,1} q \delta_{Ts,1}(R^2-(R-\delta_{Ts,1})^2)/(2\lambda H)$ and the right-hand side term by $\kappa Rq/\lambda$. The variables with subscript s represent the corresponding quantities in the steady stage here and hereafter. Thus, we have

$$u_{vs,1} \sim \frac{\kappa HR}{\left(2R\delta_{Ts,1} - {\delta_{Ts,1}}^2\right)\delta_{Ts,1}}. \tag{3.9}$$

It is noteworthy that the velocity $u_{vs,1}$ depends on Raq and S implicitly.

Assuming heat transfer and flow in the pipe enter the steady stage at time $t_{s,1}$ and inserting $t_{s,1}$ into (3.2), (3.4) and (3.6), we have

$$\delta_{Ts,1} \sim \kappa^{1/2} t_{s,1}^{1/2} \left(1 + \frac{\delta_{Ts,1}^3}{2\kappa t_{s,1} R}\right)^{1/2}, \tag{3.10}$$

$$u_{vs,1} \sim \frac{Ra_q}{S^4} \frac{\kappa^2 t_{s,1}}{R^3} \frac{\delta_{Ts,1}}{R} \tag{3.11}$$

and

$$\delta_{vs,1} \sim \nu^{1/2} t_{s,1}^{1/2} \left[\frac{\delta_{Ts,1}}{\nu^{1/2} t_{s,1}^{1/2}} + \left(\frac{R-\delta_{Ts,1}}{2R-\delta_{Ts,1}-\delta_{vs,1}}\right)^{1/2}\right] \sim \nu^{1/2} t_{s,1}^{1/2} \eta'_{vs,1}, \tag{3.12}$$

respectively.

Equation (3.10) can be written as $(2R\delta_{Ts,1} - \delta_{Ts,1}^2)\delta_{Ts,1} \sim 2R\kappa t_{s,1}$, and substituting this into (3.9) yields $u_{vs,1} \sim L/t_{s,1}$. Physically, (3.9) states the balance between heat convected away and conducted in, while (3.10) is based on the assumption of self-similar growth of the thermal boundary layer. The resulting scale $u_{vs,1} \sim L/t_{s,1}$ reflects a simple yet fundamental constraint: for a steady convection to be established from start-up, fluid parcels must travel a distance $(u_{vs,1} t_{s,1})$ comparable to several times the heated length L. Inserting $u_{vs,1} \sim L/t_{s,1}$ into (3.11), we can obtain

$$t_{s,1} \sim \left(\frac{S^5}{Ra_q} \frac{R}{\delta_{Ts,1}}\right)^{1/2} \frac{R^2}{\kappa}. \tag{3.13}$$

Using (3.10) and (3.13), $\delta_{Ts,1}$ and $t_{s,1}$ can be finally expressed as

$$\delta_{Ts,1} \sim \frac{SR}{Ra_q^{1/5}} \left[1 + \frac{1}{2} \frac{Ra_q^{1/2}}{S^{5/2}} \left(\frac{\delta_{Ts,1}}{R}\right)^{7/2}\right]^{2/5} \sim \frac{SR}{Ra_q^{1/5}} \eta_{Ts,1}, \tag{3.14}$$

$$t_{s,1} \sim \frac{S^2}{Ra_q^{2/5}} \frac{R^2}{\kappa} \eta_{Ts,1}^{-1/2}. \tag{3.15}$$

Furthermore, inserting (3.14) and (3.15) into (3.11) and (3.12) gives

$$u_{vs,1} \sim \frac{Ra_q^{2/5} \kappa}{SR} \eta_{Ts,1}^{1/2}, \tag{3.16}$$

$$\delta_{vs,1} \sim \frac{SR}{Ra_q^{1/5}} \eta_{Ts,1}^{-1/4} Pr^{1/2} \eta'_{vs,1} \sim \frac{SR}{Ra_q^{1/5}} \eta_{vs,1}. \tag{3.17}$$

https://doi.org/10.1017/jfm.2026.11695 Published online by Cambridge University Press

Based on $2\pi R\delta_{vs,1}u_{vs,1}$, the flow rate at the outlet of the pipe can be expressed as

$$Q_{os,1} \sim Ra_q^{1/5} R\kappa \eta_{Ts,1}^{1/2} \eta_{vs,1}. \tag{3.18}$$

In the fully developed stage the heat conducted from the boundary, $2\pi RHq$, balances that convected away, $\rho c_p \pi u_s \Delta T_{s,1}$, where $\Delta T_{s,1}$ is the temperature difference between the inlet and outlet. Using (3.14) and (3.16), a scaling law about $\Delta T_{os,1}$ can be written as

$$\Delta T_{os,1} \sim \frac{S}{Ra_q^{1/5}} \frac{qR}{\lambda} \eta_{Ts,1}. \tag{3.19}$$

Comparing (3.14)−(3.19) with the corresponding scaling relations for a type I fully developed boundary layer flow at $Pr < 1$ (Nie & Xu 2022) reveals that the expressions differ only in the curvature coefficients.

3.2. *Route R2*

When $\delta_{v,1}$ increases further and merges at the centre of the pipe, the flow transitions to the scenario of type II. The time scale for the merge of the viscous boundary layer, t_v, satisfies $R \sim \delta_{v,1}|_{t=t_v}$. According to (3.6), which can be simplified as $\nu^{1/2} t_v^{1/2} \eta_{v,1}/R \sim 1$ considering the fact that the velocity boundary layer is much thicker than the thermal boundary layer for water, we have

$$t_v \sim \frac{R^2}{\nu \eta_{v,1}^2}. \tag{3.20}$$

Assuming the merging of the viscous boundary layer has a negligible impact on the development of the thermal boundary layer, as the viscous boundary layer is much thicker than the thermal boundary layer and the velocity has become much weaker at the tail, this means that $\delta_{T,2}$ still follows the same scaling law as (3.2) for $\delta_{T,1}$, that is,

$$\delta_{T,2} \sim \kappa^{1/2} t^{1/2} \eta_{T,2}, \tag{3.21}$$

with $\eta_{T,2} \sim \eta_{T,1}$.

The balance of the momentum equation (2.3) is still between the viscous and buoyancy terms for the thermal boundary layer ($R - \delta_{T,2} < r < R$). As the velocity boundary layer merges at the centreline, integrated along the axial direction to obtain a global relation,

$$-\nu \int_0^L \int_{R-\delta_{T,2}}^R \frac{\partial}{\partial r}\left(r\frac{\partial u_z}{\partial r}\right) \mathrm{d}r\mathrm{d}z \sim \int_0^L \int_{R-\delta_{T,2}}^R g\beta \Delta T r \mathrm{d}r\mathrm{d}z. \tag{3.22}$$

Although the velocity boundary layer has merged at the centreline, the buoyancy force is confined within the still-distinct thermal boundary layer and drives the dominant velocity variation near the wall. The characteristic wall-normal velocity gradient $\partial u_z/\partial r$ at $r = R$ is taken as $u_{v,2}/\delta_{T,2}$. Therefore, (3.22) can be estimated as

$$\nu R \frac{u_{v,2}}{\delta_{T,2}} L + \nu (R - \delta_{T,2}) L \frac{\partial u_z}{\partial r}|_{R-\delta_{T,2}} \sim g\beta q L \delta_{T,2} (R^2 - (R - \delta_{T,2})^2)/(2\lambda). \tag{3.23}$$

In the layer $0 < r < R - \delta_{T,2}$, the balance between the viscous and inertial terms of (2.3) gives

$$\int_0^L \int_0^{R-\delta_T} r\frac{\partial u_z}{\partial t} \mathrm{d}r\mathrm{d}z \sim \nu \int_0^L \int_0^{R-\delta_T} \frac{\partial}{\partial r}\left(r\frac{\partial u_z}{\partial r}\right) \mathrm{d}r\mathrm{d}z, \tag{3.24}$$

https://doi.org/10.1017/jfm.2026.11695 Published online by Cambridge University Press

As $\partial u_z/\partial r = 0$ at $r = 0$, it can be simplified as

$$\frac{u_{v,2}}{t}\frac{(R-\delta_{T,2})^2}{2}L \sim \nu(R-\delta_{T,2})L\frac{\partial u_z}{\partial r}\,|_{R-\delta_{T,2}}\,. \tag{3.25}$$

Using (3.23) and (3.25), we have

$$u_{v,2} \sim \frac{Ra_q}{S^4}\frac{\kappa^2 t}{R^3}\frac{\delta_{T,2}}{R}\cdot\left[2+\frac{\delta_{T,2}}{R}\cdot\frac{(1-\delta_{T,2}/R)^2}{\nu t/R^2}\right]^{-1} \sim \frac{Ra_q}{S^4}\frac{\kappa^{5/2}t^{3/2}}{R^4}\eta_{T,2}. \tag{3.26}$$

The flow rate $Q_{o,2}$ can be estimated by $\pi R^2 u_T$. Using (3.26) we obtain

$$Q_{o,2} \sim \frac{Ra_q}{S^4}\frac{\kappa^3 t^2}{R}\eta_{T,2}. \tag{3.27}$$

Comparing $\delta_{T,2}$ with $\delta_{T,1}$ and $u_{v,2}$ with $u_{v,1}$, it shows that the thickness of the thermal boundary layer and the typical velocity in the scenario of unsteady type II develop as the same laws as that of the scenario of unsteady type I. This implies that the emergence of the velocity boundary layer introduces only a secondary effect on the development of the temperature boundary layer and the subsequent buoyancy-driven forces.

The flow and heat transfer become fully developed once the heat convected away balances that conducted in. As the velocity boundary layer merges at the centre, $\delta_{vs,2}$ remains at R. Repeating the discussion of (3.8)–(3.15), the velocity and time scales in the fully developed stage read

$$\frac{\delta_{Ts,2}}{R} \sim \frac{S}{Ra_q^{1/5}}\left[1+\frac{1}{2}\frac{Ra_q^{1/2}}{S^{5/2}}\left(\frac{\delta_{Ts,2}}{R}\right)^{7/2}\right]^{2/5} \sim \frac{S}{Ra_q^{1/5}}\eta_{Ts,2} \tag{3.28}$$

and

$$t_{s,2} \sim \frac{S^2}{Ra_q^{2/5}}\frac{R^2}{\kappa}\eta_{Ts,2}^{-1/2}. \tag{3.29}$$

respectively.

Repeating the discussion about $u_{vs,1} \sim L/t_{s,1}$ based on (3.9) and (3.10), we have $u_{vs,2} \sim L/t_{s,2}$. The similarity arises because only the thicker velocity boundary layer merges, with merely a secondary effect on thermal growth and buoyancy. Then, the scale for the velocity reads

$$u_{vs,2} \sim \frac{Ra_q^{2/5}}{S}\frac{\kappa}{R}\eta_{Ts,2}^{1/2}. \tag{3.30}$$

Based on $\pi R^2 \delta_{vs} u_{qs}$, the flow rate at the outlet of the pipe can be expressed as

$$Q_{os,2} \sim \frac{Ra_q^{2/5}}{S}\kappa R\eta_{Ts,2}^{1/2}. \tag{3.31}$$

Repeating the discussion of (3.19) gives $\rho c_p \pi(R^2-(R-\delta_{Ts,2})^2)u_{vs,2}\Delta T_{os,2} \sim 2\pi RHq$. Accordingly, the scale of the temperature difference between the inlet and outlet can be written as

$$\Delta T_{os,2} \sim \frac{S}{Ra_q^{1/5}}\frac{qR}{\lambda}\eta_{Ts,2}. \tag{3.32}$$

https://doi.org/10.1017/jfm.2026.11695 Published online by Cambridge University Press

3.3. *Route R3*

The merged thermal boundary layer and pipe flow develop from the unsteady stage of type II. When the thermal boundary layer increases and merges at the centre, $\delta_{T,3}$ is limited at R. The time scale for the merge of the thermal boundary layer, t_s, satisfies $R \sim \delta_{T,1}|_{t=t_s}$ as $\delta_{T,1}$ and $\delta_{T,2}$ follow the same relation. As (3.2) can be rewritten as $(\delta_T/R)^2 \sim \kappa t_T/R^2 + 1/2(\delta_T/R)^3$ and is further simplified to $\kappa t_T/R^2 \sim 0.5$, we have

$$t_T \sim \frac{R^2}{\kappa}. \tag{3.33}$$

For the pipe flow, the balance of the momentum equation (2.3) is still between the viscous and buoyancy terms:

$$-\nu \int_0^L \int_0^R \frac{\partial}{\partial r}\left(r\frac{\partial u_z}{\partial r}\right) \mathrm{d}r\mathrm{d}z \sim \int_0^L \int_0^R g\beta\Delta T r \mathrm{d}r\mathrm{d}z. \tag{3.34}$$

As the $\partial u_z/\partial r = 0$ at $r = 0$, the left-hand side term can be estimated by $1/2\nu u_{v,3}L$. The right-hand side term can be estimated by $1/2g\beta\Delta T R^2 L$. Considering that most of the heat conducted in, $2\pi RLqt$, is converted into the internal energy of the water, $\rho c_p \pi R^2 L\Delta T$, the right-hand side term can be further simplified as $Ra_q\kappa^2\nu Rt/L^4$. Therefore, (3.34) can be simplified as

$$u_{v,3} \sim \frac{Ra_q}{S^4}\frac{\kappa^2}{R^3}t. \tag{3.35}$$

Accordingly, the flow rate estimated by $\pi R^2 u_{v,3}$ reads

$$Q_{o,3} \sim \frac{Ra_q}{S^4}\frac{\kappa^2}{R}t. \tag{3.36}$$

In the fully developed stage the heat conducted in will be convected away, that is, $\rho c_p \pi R^2 u_{vs,3}\Delta T_{os,3} \sim 2\pi RHq$. We have

$$\Delta T_{os,3} \sim \frac{\kappa Hq}{\lambda R u_{vs,3}}. \tag{3.37}$$

Equation (3.34) is still valid for the fully developed stage:

$$\nu u_{vs,3} \sim g\beta\Delta T_{os,3}R^2. \tag{3.38}$$

Using (3.37) and (3.38), the scaling law of velocity and temperature difference can be written as

$$u_{vs,3} \sim \frac{Ra_q^{1/2}}{S^{3/2}}\frac{\kappa}{R} \tag{3.39}$$

and

$$\Delta T_{os,3} \sim \frac{S^{5/2}}{Ra_q^{1/2}}\frac{qR}{\lambda}, \tag{3.40}$$

respectively.

Based on (3.39), the flow rate can also be estimated as

$$Q_{os,3} \sim \frac{Ra_q^{1/2}}{S^{3/2}}\kappa R. \tag{3.41}$$

https://doi.org/10.1017/jfm.2026.11695 Published online by Cambridge University Press

Stages	Quantities	Regimes		
		R1	R2	R3
Steady	Thermal layer thickness	(3.2)	(3.21)	$\sim R$
	Velocity layer thickness	(3.6)	$\sim R$	$\sim R$
	Velocity	(3.4)	(3.26)	(3.35)
	Flow rate	(3.7)	(3.27)	(3.36)
Transition time		(3.15)	(3.29)	(3.42)
Unsteady	Thermal layer thickness	(3.14)	(3.28)	$\sim R$
	Velocity layer thickness	(3.12)	$\sim R$	$\sim R$
	Velocity	(3.16)	(3.30)	(3.39)
	Flow rate	(3.18)	(3.31)	(3.41)
	Temperature	(3.19)	(3.32)	(3.40)

Table 1. Summary of the scaling laws for natural convection in a pipe with a fluid of $Pr > 1$.

Using (3.35) and (3.39), the time scale for the flow to develop into the steady type III regime can be written as

$$t_{s,3} \sim \frac{S^{5/2}}{Ra_q^{1/2}} \frac{R^2}{\kappa}. \tag{3.42}$$

3.4. *Regimes*

The criterion for route R1 is $t_{s,1} \leqslant t_v$, for route R2 is $t_v < t_{s,2} \leqslant t_T$ and for route R3 is $t_{s,3} > t_T$. According to (3.15), (3.29) and (3.42), $t_{s,1}/(R^2/\kappa)$, $t_{s,2}/(R^2/\kappa)$ and $t_{s,3}/(R^2/\kappa)$ are functions of S^5/Ra_q. Considering (3.20) and (3.33), the criteria distinguishing the three routes are

$$\text{Routes} \begin{cases} \text{R1}: Ra_q \geqslant I_{c,12} S^5, \\ \text{R2}: I_{c,12} S^5 < Ra_q \leqslant I_{c,23} S^5, \\ \text{R3}: Ra_q > I_{c,23} S^5. \end{cases} \tag{3.43}$$

Here, $I_{c,12}$ and $I_{c,23}$ are some critical values and can be determined by numerical or physical experiments.

The scales obtained in §§ 3.1–3.3 for the three regimes are summarised in table 1.

3.5. *Curvature effect*

In our previous paper (Nie & Xu 2022), the curvature effects for a non-merged thermal boundary layer adjacent to a vertical pipe wall were discussed and compared with those on a flat vertical wall; however, that analysis was limited to fluids with $Pr < 1$, for which the thermal and velocity boundary layers are of equal thickness. In the present study, we focus on the case of $Pr > 1$ and have derived the corresponding curvature coefficients quantifying the wall curvature effect on the flow and heat transfer in § 3.1.

The main findings regarding wall curvature effects from § 3.1 are summarised as follows. (i) In the unsteady stage, the curvature effects are quantified by the coefficients $\eta_{T,1}$ for the thermal boundary layer thickness (3.2), $\eta_{v,1}$ for the velocity boundary layer thickness (3.6), $\eta_{T,1}$ for the velocity (3.4) and $\eta_{T,1}\eta_{v,1}$ for the flow rate (3.7). (ii) In the fully developed stage, the corresponding effects are quantified by $\eta_{Ts,1}$ for the thermal boundary layer thickness (3.14), $\eta_{vs,1}$ for the velocity boundary layer thickness (3.17), $\eta_{Ts,1}^{1/2}$ for the velocity (3.16) and $\eta_{Ts,1}^{1/2}\eta_{vs,1}$ for the flow rate (3.18).

https://doi.org/10.1017/jfm.2026.11695 Published online by Cambridge University Press

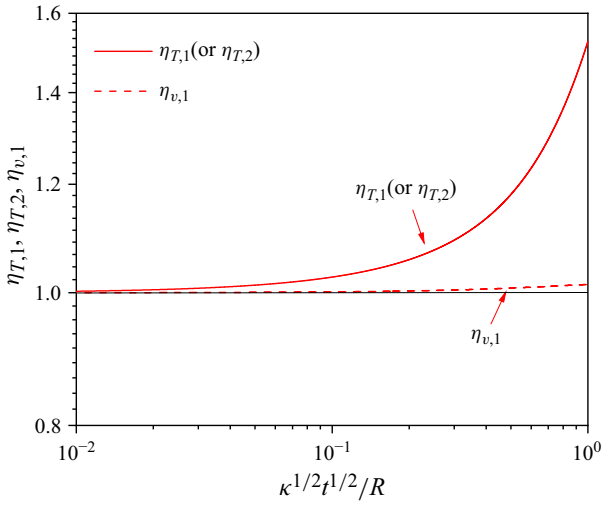


Figure 4. Dependence on $\kappa^{1/2}t^{1/2}/R$ of the curvature coefficients for the scenarios of unsteady type I and type II.

A comparison with our previous paper (Nie & Xu 2022) shows that the curvature effect on the thermal boundary layer thickness and the velocity remains the same in the unsteady stage for both $Pr < 1$ and $Pr > 1$. However, the curvature effect has no influence on the flow rate for $Pr < 1$ but enhances it by a factor of $\eta_{T,1}\eta_{v,1}$ for $Pr > 1$. This is because the flow rate is determined by the velocity boundary layer thickness. While the velocity and thermal boundary layer thicknesses are equal for $Pr < 1$, this is not the case for $Pr > 1$.

In contrast to flat vertical walls, the type II and type III scenarios for $Pr > 1$ discussed in §§ 3.2 and 3.3, respectively, arise entirely due to the curvature effect of the wall. They also differ from the $Pr < 1$ case, in which the thermal and velocity boundary layers merge simultaneously. For the type II scenario, the curvature effect in the unsteady stage is quantified by $\eta_{T,2}$ for the thermal boundary layer thickness (3.21), velocity (3.26) and flow rate (3.27). In the fully developed stage, the corresponding effects are quantified by $\eta_{Ts,2}$ for the thermal boundary layer thickness (3.28), $\eta_{Ts,2}^{1/2}$ for the velocity (3.30) and $\eta_{Ts,2}^{1/2}$ for the flow rate (3.31).

We now examine the curvature coefficients: $\eta_{T,1}$, $\eta_{v,1}$ and $\eta_{T,1}\eta_{v,1}$. Since $\eta_{T,1}$ and $\eta_{v,1}$ are functions of $\kappa^{1/2}t^{1/2}/R$ according to (3.2) and (3.6), these coefficients are plotted against this dimensionless time in figure 4. The curvature coefficient $\eta_{T,2}$ for the unsteady type II scenario, which has the same functional form as $\eta_{T,1}$, is also presented. Similarly, we examine the coefficients for the fully developed stage: $\eta_{Ts,1}$, $\eta_{vs,1}$, $\eta_{Ts,1}^{1/2}$ and $\eta_{Ts,1}^{1/2}\eta_{vs,1}$. As $\eta_{Ts,1}$ and $\eta_{vs,1}$ are functions of $SRa_q^{-1/5}$ according to (3.14) and (3.17), these coefficients are plotted against this parameter in figure 5. The curvature coefficient $\eta_{Ts,2}$ for the scenario of steady type II is also shown. Figures 4 and 5 show that the curvature effect is comparable in magnitude to the leading-order term and increases with the thickness of the boundary layers. Accordingly, its impact is significant and can be quantitatively assessed.

4. Thermal plume

The thermal plume originating from the pipe ascends until it reaches the free surface, a process strongly dependent on the flow regime within the pipe. In this section the thermal

https://doi.org/10.1017/jfm.2026.11695 Published online by Cambridge University Press

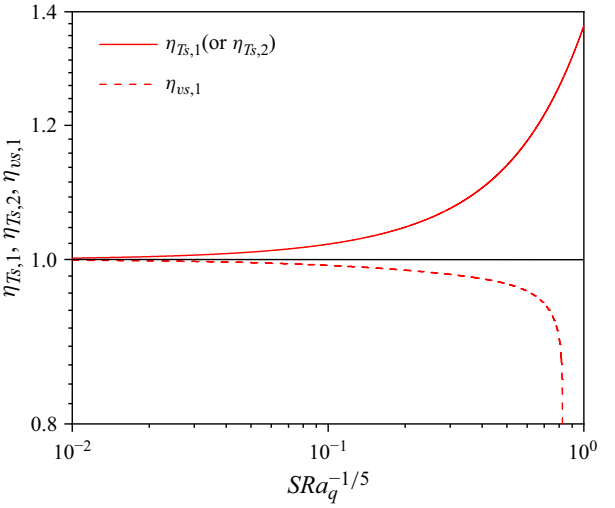


Figure 5. Curvature coefficients for the scenarios of fully developed type I and type II.

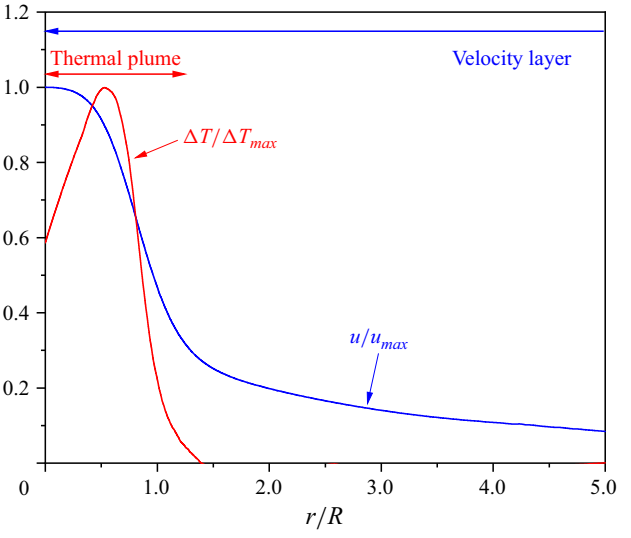


Figure 6. Typical temperature and velocity profiles for the thermal plume. The profiles shown are the numerical results of the case $Ra_q = 10^6$, $S = 6.0$ and $D = 4.00$ at $z = L + H/2$.

plume in the fully developed stage caused by the flow of type III in the pipe is investigated. We focus on this scenario due to its higher capacity for vertical mass transport.

The typical temperature and velocity profiles of the plume are shown in figure 6. Under the assumption of axisymmetry, the plume can be characterised by two regions: a thermal plume flow layer $0 < r < \delta_{Tps,3}$ and a viscous layer $\delta_{Tps,3} < r < \delta_{vps,3}$.

The plume's heat supply originates solely from the isoflux pipe wall. Conservation of energy requires that the heat convected by the plume balances the heat conducted from the boundary, which suggests that

$$\rho c_p \pi \delta_{Tps,3}^2 u_{ps,3} \Delta T_{ps,3} \sim 2\pi RLq. \tag{4.1}$$

https://doi.org/10.1017/jfm.2026.11695 Published online by Cambridge University Press

Here, $u_{ps,3}$ is the characteristic velocity of the plume; $\Delta T_{ps,3} = T_{ps,3} - T_0$ is the characteristic temperature difference of the plume relative to the ambient.

The flow in the layer, $\delta_{Tps} < r < \delta_{vps}$, is driven by the viscous shear owing to the larger speed of the thermal plume. The balance of the momentum equation for this layer is between the viscous term and the advection term:

$$\nu \int_{\delta_{Tps,3}}^{\delta_{vps,3}} \frac{\partial}{\partial r}\left(r\frac{\partial u_z}{\partial r}\right) \mathrm{d}r \sim \int_{\delta_{Tps,3}}^{\delta_{vps,3}} u_z \frac{\partial u_z}{\partial z} r \mathrm{d}r. \tag{4.2}$$

As $\partial u_z/\partial r$ is nearly zero at $r = \delta_{vps,3}$, it can be simplified to

$$\frac{\nu \delta_{Tps,3}}{\delta_{vps,3}} \sim \frac{u_{vs,3}}{H} \frac{(\delta_{vps,3})^2 - (\delta_{Tps,3})^2}{2}. \tag{4.3}$$

The thermal plume layer, $0 < r < \delta_{Tps,3}$, is driven by the buoyancy force. As the plume comes from the pipe flow, and the viscous term is always larger than the inertial term for the pipe flow, it implies that the buoyancy term is balanced by the viscous term for the plume, i.e.

$$\int_0^{\delta_{TPs,3}} g\beta(T - T_0) r \mathrm{d}r \sim -\nu \int_0^{\delta_{TPs,3}} \frac{\partial}{\partial r}\left(r\frac{\partial u_z}{\partial r}\right) \mathrm{d}r. \tag{4.4}$$

As $\partial u_z/\partial r$ is zero at $r = 0$, it can be simplified as

$$g\beta \Delta T_{ps,3} \frac{\delta_{TPs,3}}{2} \sim \nu \frac{u_{ps,3}}{\delta_{vps,3}}. \tag{4.5}$$

The heat transfer of the plume in the radial direction results in the expansion of the thermal plume. The rate of this radial heat transfer can be estimated as $2\pi R H \lambda \Delta T_{ps,3}/\delta_{Tps,3}$. As the plume rises with its energy conserved, the decrease in the streamwise advective heat flux of the plume core is balanced by the radial heat transfer. The decrease of streamwise heat transfer of the plume core can be estimated by $c\rho u_{vs,3}\pi R^2 \Delta T_{os,3} - c\rho u_{ps,3}\pi R^2 \Delta T_{ps,3}$ when it is dominated by advection. As $c\rho u_{vs,3}\pi R^2 \Delta T_{os,3}$ is always larger than $c\rho u_{ps,3}\pi R^2 \Delta T_{ps,3}$, we have

$$2\pi R H \lambda \Delta T_{ps,3}/\delta_{Tps,3} \sim c\rho u_{vs,3}\pi R^2 \Delta T_{os,3}. \tag{4.6}$$

Eliminating $\Delta T_{ps,3}$ in (4.1), (4.5) and (4.6) yields

$$(\delta_{Tps,3})^3 u_{ps,3} \sim \frac{LHq\kappa^2}{\lambda u_{vs,3} \Delta T_{os,3}} \tag{4.7}$$

and

$$\frac{u_{ps,3}\delta_{vps,3}}{\delta_{TPs,3}^2} \sim \frac{g\beta R}{H\kappa\nu} u_{vs,3} \Delta T_{os,3}. \tag{4.8}$$

Eliminating $u_{ps,3}$ in (4.7) and (4.8), and using the results of $u_{vs,3}$ (3.39), and $\Delta T_{os,3}$ (3.40), we derive a relation of the thickness of thermal and viscous layers of the plume as

$$\delta_{Tps,3}^5 \delta_{vps,3} \sim \frac{D^2 S^3}{Ra_q} R^6. \tag{4.9}$$

Using (3.39) and considering $\delta_{vps,3}$ is always larger than $\delta_{Tps,3}$ for $Pr = 7$, (4.3) can be written as

$$\delta_{vps,3}\delta_{Tps,3}[(\delta_{vps,3}/\delta_{Tps,3})^2 - 1] \sim \delta_{vps,3}^3/\delta_{Tps,3} \sim \frac{S^{3/2} D}{Ra_q^{1/2}} R^2. \tag{4.10}$$

https://doi.org/10.1017/jfm.2026.11695 Published online by Cambridge University Press

From (4.9) and (4.10), we fint that

$$\delta_{Tps,3} \sim \frac{D^{5/16} S^{15/32}}{Ra_q^{5/32}} R \tag{4.11}$$

and

$$\delta_{vps,3} \sim \frac{D^{7/16} S^{21/32}}{Ra_q^{7/32}} R. \tag{4.12}$$

Substituting (4.11), (3.39) and (3.40) into (4.6) gives the typical temperature of the plume:

$$\Delta T_{ps,3} \sim \frac{S^{47/32}}{D^{11/16} Ra_q^{5/32}} \frac{qR}{\lambda}. \tag{4.13}$$

Furthermore, the typical velocity of the plume can also be obtained using (4.1), (4.11) and (4.13) as

$$u_{ps,3} \sim \frac{D^{1/16} Ra_q^{15/32}}{S^{45/32}} \frac{\kappa}{R}. \tag{4.14}$$

For an unbounded laminar plume, the vertical velocity scales as $Ra_q^{1/2} S^{3/2} \kappa / R$ (Batchelor 1954; Kaminski & Jaupart 2003), in which the power input in the original theory has been expressed as $2\pi RLq$. Our scaling yields exponents of 0.47 for Ra_q and 1.4 for S, which are very close to 0.5 and 1.5 in the classical scaling. This slight discrepancy is likely attributable to the blocking effect of the upper free surface on the rising plume, which is not accounted for in classical unconfined-plume scalings.

According to $\pi \delta_{vps,3}^2 u_{ps,3}$, the flow rate $Q_{ps,3}$ can be written as

$$Q_{ps,3} \sim \frac{D^{15/16} Ra_q^{1/32}}{S^{3/32}} \kappa R. \tag{4.15}$$

5. Radial intrusion flow

When the ascending plume impinges on the free surface, its vertical momentum is rapidly converted, leading to a stagnation region. The transport of heat and momentum of the intrusion flow is inhibited in the vertical direction due to the buoyancy effect. This results in a significant pressure increase, which drives a radial intrusion flow. Thus, the vertical gradients of temperature and velocity are much larger than those in the radial and circumferential directions.

Spatially, the intrusion flow may be divided into the following three regions: (i) impinging region ($r \leqslant r_{pg}$): the direction of streamlines turns from vertical to horizontal, and the radial current driven by the radial pressure difference balanced by the convection term experiences a significant acceleration; (ii) spreading region ($r_{pg} < r \leqslant r_{tl}$): the radial spreading flow decelerates and the kinetic energy of the radial current is consumed gradually; (iii) tail region ($r > r_{tl}$): a distinct intrusion flow cannot be observed and the radial heat transfer is dominated by conduction rather than convection. The critical radii r_{pg} and r_{tl} will be discussed later.

https://doi.org/10.1017/jfm.2026.11695 Published online by Cambridge University Press

5.1. *Impinging*

The volume of fluid entrained in the impinging region is much less than $Q_{ps,3}$. Therefore, the flow rate at the exit of the impinging region scales with $Q_{ps,3}$, which gives

$$2\pi r_{pg}\delta_{Is0,3}u_{Is0,3} \sim Q_{ps,3}. \tag{5.1}$$

Here, $\delta_{Is0,3}$ and $u_{Is0,3}$ are the thickness and velocity of the thin-layer intrusion flow at $r = r_{pg}$, respectively.

The pressure increase in the vertical direction, Δp, for buoyancy-driven flow can be estimated as $\rho g\beta\Delta T_{ps,3}\delta_{Is0,3}$. In the radial momentum equation, the pressure term $(-1/\rho\partial P/\partial r)$ is balanced by the convection term $(u_r\partial u_r/\partial r)$ due to the intense acceleration. The radial flow driven by the pressure difference can thus be written as

$$\frac{u_{Is0,3}^2}{r_{pg}} \sim \frac{1}{\rho}\frac{\Delta P}{r_{pg}} \sim \frac{1}{\rho}\frac{\rho g\beta\Delta T_{ps,3}\delta_{Is0,3}}{r_{pg}}. \tag{5.2}$$

By combining the flow rate constraint (5.1) and the momentum balance (5.2), and substituting the scalings for the plume temperature (4.13) and flow rate (4.15), we derive the following scaling laws for the intrusion flow at $r = r_{pg}$:

$$\delta_{Is0,3} \sim \frac{D^{41/48}S^{25/32}}{Ra^{25/96}}\frac{R^{5/3}}{r_{pg}^{2/3}}, \tag{5.3}$$

$$u_{Is0,3} \sim \frac{D^{1/12}Ra^{7/24}}{S^{7/8}}\frac{\kappa}{r_{pg}^{1/3}R^{2/3}}. \tag{5.4}$$

Consequently, the axisymmetric intrusion flows with a thickness of $\delta_{Is0,3}$ and a velocity of $u_{Is0,3}$ are formed. Considering the mixing in the impinging region, the temperature of the intrusion flow is assumed to be quasi-uniform and scales with $\Delta T_{ps,3}$.

5.2. *Spreading*

The driving force of a spreading intrusion flow varies. For subcritical flows (discharge Froude number $Fr \sim 1$ or less), such as oil spilling at sea (Hoult 1972) or spreading of lighter current along the free surface (Didden & Maxworthy 1982), discharging heavier current at the bottom (Huppert 1982; Bonnecaze, Huppert & Lister 1993), the flow is typically buoyancy-driven (or gravity driven). In contrast, supercritical horizontal buoyant jets are primarily inertia-driven (Didden & Maxworthy 1982). In our scenario, the Froude number of the spreading flow is estimated as $Fr \sim u_{Is0,3}(g\beta\Delta T_{ps,3}\delta_{Is0,3})^{-1/2}$. Inserting (5.3), (5.4) and (4.13), Fr is only a function of the Prandtl number and independent of Ra_q, S or D. Considering the thermal plume and flow in the impinging region fall in the buoyancy force-driven flow regime, it confirms that the buoyancy force drives the spreading flow.

The opposing force that balances buoyancy can be either viscous or convection terms, depending on the local Reynolds number (Re). It is noteworthy that the role of the convection term evolves with the flow process. In the impinging region the convection term balances the driving force, buoyancy-driven pressure gradient, resulting in flow acceleration. In the spreading region the flow decelerates as the viscous term balances the convection term, in which now convection acts as the driving mechanism. Accordingly, the transition from a convection-dominated impinging region to a viscous-dominated spreading region occurs at r_{pg}. Using (5.3) and (5.4), and applying the criterion $Re \sim 1$,

https://doi.org/10.1017/jfm.2026.11695 Published online by Cambridge University Press

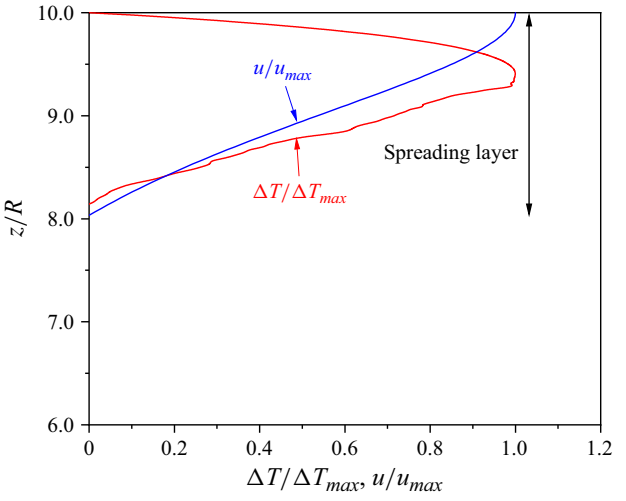


Figure 7. Typical temperature and velocity profiles for the intrusion flow. The profiles shown are the numerical results of the case $Ra_q = 10^6$, $S = 6.0$ and $D = 4.00$ at $r = 2.0R$.

i.e. $u_{Is0,3}\delta_{Is0,3}/\nu$ is unity, gives

$$r_{pg} \sim \frac{Ra^{1/32}D^{15/16}}{S^{3/32}}R. \tag{5.5}$$

We adopt a one-layer model for the spreading flow, as buoyancy confines heat and momentum transport in the vertical direction. Let $\delta_{Is,3}$ and $u_{Is,3}$ denote the thickness and velocity of the spreading current, respectively, as shown in figure 7. For simplicity, a local coordinate downward with $z' = 0$ at the free surface is used for the discussion of the spreading flow.

The balance of the buoyancy-driven pressure difference and viscous force suggests that

$$\int_0^{\delta_{Is,3}} \frac{g\beta\Delta T_{ps,3}\delta_{Is,3}}{r}\mathrm{d}z' \sim \nu\int_0^{\delta_{Is,3}} \frac{\partial^2 u_r}{\partial z'^2}\mathrm{d}z'. \tag{5.6}$$

Substituting the scaling for $\Delta T_{ps,3}$ from (4.13) and using the definition of Ra_q to simplify, (5.6) can be expressed as

$$\frac{Ra^{27/32}}{D^{11/16}S^{81/32}}\frac{\nu\kappa}{R^3}\frac{\delta_{Is,3}^2}{r} \sim \nu\frac{u_{Is,3}}{\delta_{Is,3}}. \tag{5.7}$$

Conservation of the flow rate gives

$$u_{Is,3}2\pi r\delta_{Is,3} \sim Q_{ps,3}, \tag{5.8}$$

in which $Q_{ps,3}$ has already been given in (4.15).

With (5.7) and (5.8), we can have the thickness and velocity of the spreading flow at r as

$$u_{Is,3} \sim \frac{D^{17/32}Ra^{15/64}}{S^{45/64}}\frac{\kappa}{r}, \tag{5.9}$$

$$\delta_{Is,3} \sim \frac{S^{39/64}D^{13/32}}{Ra^{13/64}}R. \tag{5.10}$$

https://doi.org/10.1017/jfm.2026.11695 Published online by Cambridge University Press

Case runs	Height/radius	Rayleigh number	Depth/radius
01–04	$S = 0.1$	$Ra_q = 10^4, 10^5, 10^6, 10^7$	$D = 1.3$
05–08	$S = 0.5$	$Ra_q = 10^4, 10^5, 10^6, 10^7$	
09–12	$S = 2.0$	$Ra_q = 10^4, 10^5, 10^6, 10^7$	
13–16	$S = 4.0$	$Ra_q = 10^4, 10^5, 10^6, 10^7$	
17–20	$S = 6.0$	$Ra_q = 10^4, 10^5, 10^6, 10^7$	
21–24	$S = 0.1$	$Ra_q = 10^4, 10^5, 10^6, 10^7$	$D = 4.0$
25–28	$S = 0.5$	$Ra_q = 10^4, 10^5, 10^6, 10^7$	
29–32	$S = 2.0$	$Ra_q = 10^4, 10^5, 10^6, 10^7$	
33–36	$S = 4.0$	$Ra_q = 10^4, 10^5, 10^6, 10^7$	
37–40	$S = 6.0$	$Ra_q = 10^4, 10^5, 10^6, 10^7$	
41–42	$S = 6.0$	$Ra_q = 10^4, 10^7$	$D = 8.0$

Table 2. Parameters of numerical cases. Here $Pr = 7.0$ in all cases.

The radial position r_{tl}, marking the transition to a conduction-dominated tail region, is found by balancing advective and conductive heat transfer. The advective heat flux scales as $\rho c_p 2\pi r \delta_{Is,3} u_{Is,3} \Delta T_{ps,3}$, while the conductive rate is $2\pi r \delta_{Is,3} \cdot \lambda \Delta T_{ps,3}/\delta_{Is,3}$. Using (5.9) and (5.10), the balance of conduction and convection gives

$$r_{tl} \sim \frac{Ra^{1/32} D^{15/16}}{S^{3/32}} R. \tag{5.11}$$

In summary, the intrusion flow transitions between distinct dynamical regimes. The impinging region ($r \leqslant r_{pg}$) is characterised by a buoyancy-inertia balance, while the spreading region ($r_{pg} < r \leqslant r_{tl}$) is governed by a buoyancy-viscosity balance. Heat transfer remains advection-dominated in both the impinging and spreading regions, transitioning to conduction dominance only in the tail region ($r > r_{tl}$). Equations (5.5) and (5.11) also indicate the non-dimensional length scale (normalised by R) of the impinging region and spreading region is proportional to $Ra^{1/32} D^{15/16} S^{-3/32}$.

6. Comparison with numerical simulations

We performed a total of 42 numerical simulations to validate the scaling laws, covering the parameter ranges of $S = 0.1$–6.0, $Ra_q = 10^4$–10^7 and $D = 1.3$–8.0, as detailed in table 2. All simulations used water as the working fluid, fixing the Prandtl number at $Pr = 7.0$. The details on the numerical set-up are provided in Appendix A. Throughout this parameter space, the maximum Reynolds number of the plume is less than the critical Reynolds number for the onset of instability in a circular jet, which is approximately 500 (Gohil, Saha & Muralidhar 2012), and the maximum Froude number of the spreading flow is much less than unity.

6.1. *Flow in the pipe*

The parameter space of Ra_q-S-D can be divided into three regimes corresponding to the routes R1, R2 and R3 according to the flow within the pipe. There exists a critical value D_c, beyond which a further increase in D ceases to have a significant influence on the pipe flow. Figure 8 shows that the boundaries between regimes R2 and R3 are nearly identical for both $D = 1.3$ and $D = 4.0$. This suggests that the critical value D_c is likely less than

https://doi.org/10.1017/jfm.2026.11695 Published online by Cambridge University Press

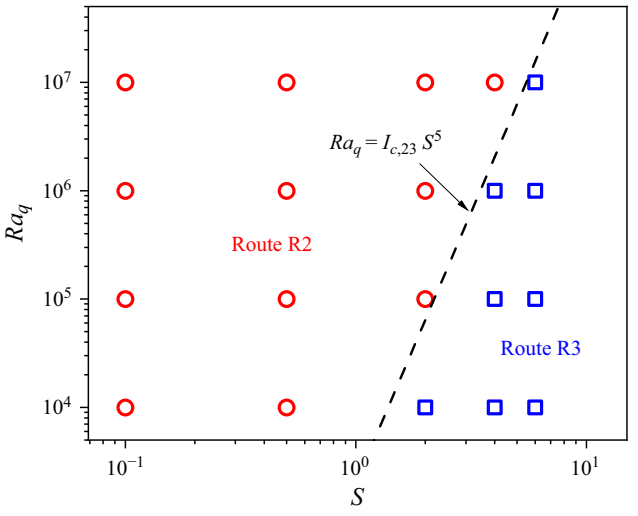


Figure 8. Regimes of the flow in the pipe in the parameter space Ra_q-S-D. Cases following route R2 are shown by the red cycle, whereas blue squares represent the cases undergoing route R3. The dashed line represents the regime boundary according to (3.43) with $I_{c,23} = 2000$. Note that this regime map is valid for the case runs 10–20 and 20–40, it implies that variation of D from 1.3 to 4.0 does not change the division of the regimes.

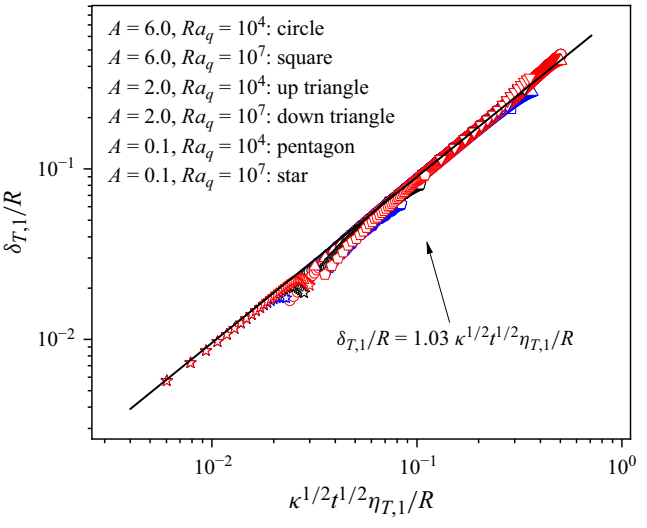


Figure 9. Variation of the thicknesses of the temperature boundary layer in the pipe over time in the start-up stage. The blue, black and red scatters are numerical results at $z/L = 0.25$, 0.5 and 0.75, respectively. The thickness of the thermal boundary layer with the solid line corresponds to the scaling law (3.2).

1.3. According to the criteria in (3.43), the flow transitions from route R3 to R2 when Ra_q increases to approximately $2000S^5$.

The scaling laws for the transient boundary layer flow during the start-up stage are validated in figure 9–11. As the transient boundary layer development is negligibly affected by variations in D from 1.3 to 8, we used data from numerical runs with $D = 1.3$ for this analysis.

The temperature profile at $z/L =$ 0.25, 0.50 and 0.75 are monitored in each case. The thermal boundary layer thickness $\delta_{T,1}$ for representative cases ($S = 0.1$, 2.0, 6.0;

https://doi.org/10.1017/jfm.2026.11695 Published online by Cambridge University Press

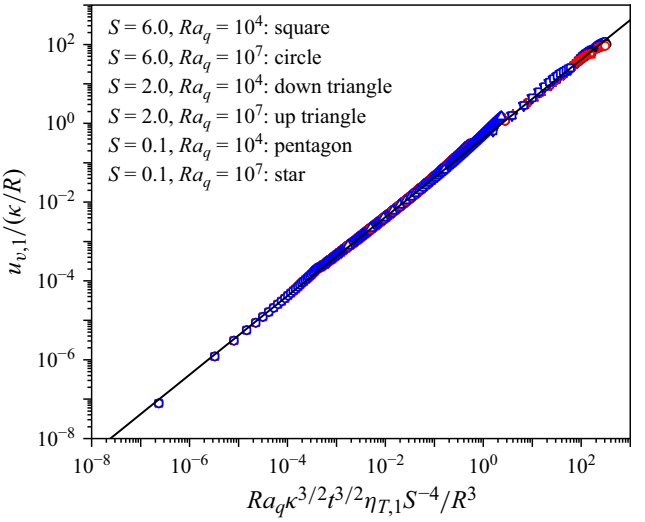


Figure 10. Variation of the maximal velocity of flow in the pipe over time in the start-up stage. The blue, black and red scatters are numerical results at $z/L = 0.25$, 0.5 and 0.75, respectively. The solid line represents the scaling law (3.4) with a proportional coefficient of 0.42.

$Ra_q = 10^4, 10^7$) is presented in figure 9. This thickness is quantified using an integral measure to avoid discrepancies from arbitrary truncation of the temperature profile tail, which is defined as

$$\delta_{T,1} = \frac{\int_0^R (T(r,t) - T_0)\mathrm{d}r}{T_w - T_0}. \tag{6.1}$$

Figure 9 shows that the numerical results for the equivalent thicknesses of the temperature boundary layer collapse onto the line predicted by (3.2), which has a slope of 1.03. The variation in thickness between different axial locations ($z/L = 0.25$, 0.50 and 0.75) is negligible. This means that the thickness along the pipe is almost uniform in the start-up stage, which is consistent with the fact that heat conduction dominates over convection initially.

Figure 10 shows the numerical results of the maximal velocity in the velocity boundary layer. The data follow the linear relation predicted by the scaling law (3.4). The velocities at all three monitored heights ($z/L = 0.25$, 0.50, 0.75) collapse onto the same line, again reflecting the weak convective effect and the resulting axial uniformity in the start-up stage.

The flow rates at the outlet of the pipe are shown in figure 11. The numerical results show that there is a linear relation between $Q_1/(\kappa R)$ and $Ra_q S^{-4}\eta_{T,1}\eta_{v,1}\kappa^2 t^2/R^4$. Discrepancies between the data and the scaling law arise from two sources. In the very early stages, the grid resolution is limited compared with the extreme thin velocity boundary layer. At later times, the deviation occurs as the flow begins its transition toward the fully developed regime. The observed scaling coefficient is larger than unity because the flow rate estimate $Q_{o,1} \sim 2\pi R\delta_{v,1}u_{v,1}$ used in the derivation omits the factor of 2π, which is subsequently absorbed into the final fitted coefficient.

In general, the thickness, maximal velocity and flow rate during the start-up stage show excellent agreement with the numerical results, as evidenced by the close match in figures 9–11. The near-uniform profiles along the pipe axis and the dominance of heat

https://doi.org/10.1017/jfm.2026.11695 Published online by Cambridge University Press

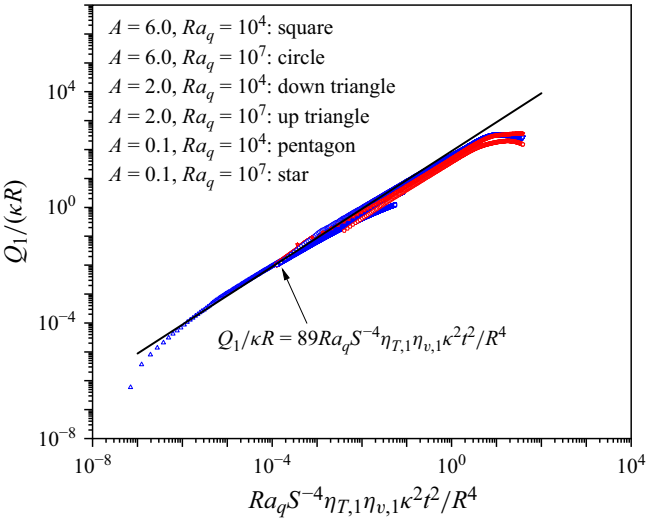


Figure 11. Variation of flow rate at the outlet of the pipe over time in the start-up stage. The solid line represents the scaling law (3.7).

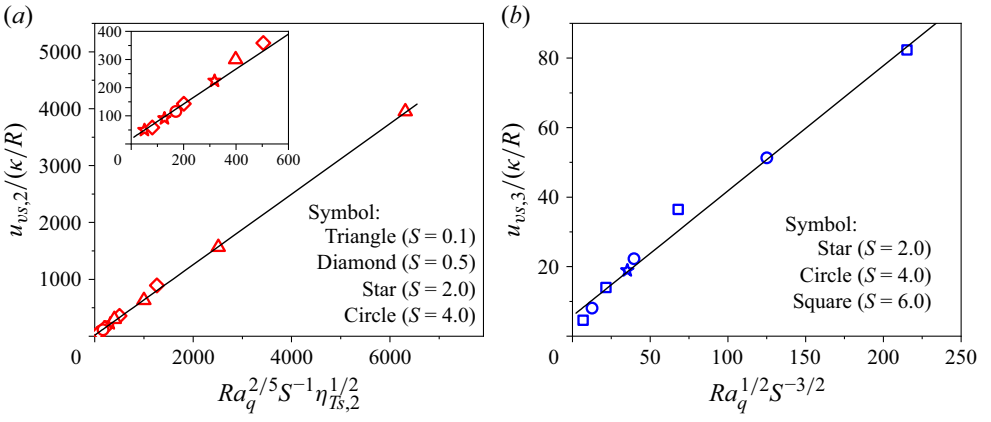


Figure 12. Maximal velocity of flow in the pipe in the fully developed stage. The scatters are numerical results monitored at the $z/L = 0.75$. (*a*) Cases in regime R2 with the solid line corresponding to the scaling law (3.30). (*b*) Cases in regime R3 with the solid line corresponding to the scaling law (3.39).

conduction over convection are consistent with the physical assumptions underlying these scaling laws.

We now present the validation of the scaling laws for the fully developed flow inside the pipe. As the velocity boundary layer in regime R2 and the temperature and velocity boundary layers in regime R3 have merged (with their thicknesses of the order of the pipe radius R), the validation focuses on the global flow parameters: the outlet velocity, flow rate and temperature difference, as shown in figure 12–14.

The maximal velocities of the numerical cases in regime R2 and regime R3 are collected separately when the heat transfer and flow are fully developed. Figure 12(*a*) shows the maximal velocities for regime R2, in which the velocity boundary layer has merged at the centre but the thermal boundary layer has not. The non-dimensional velocities collapse onto the line predicted by the scaling law (3.30). The numerical results

https://doi.org/10.1017/jfm.2026.11695 Published online by Cambridge University Press

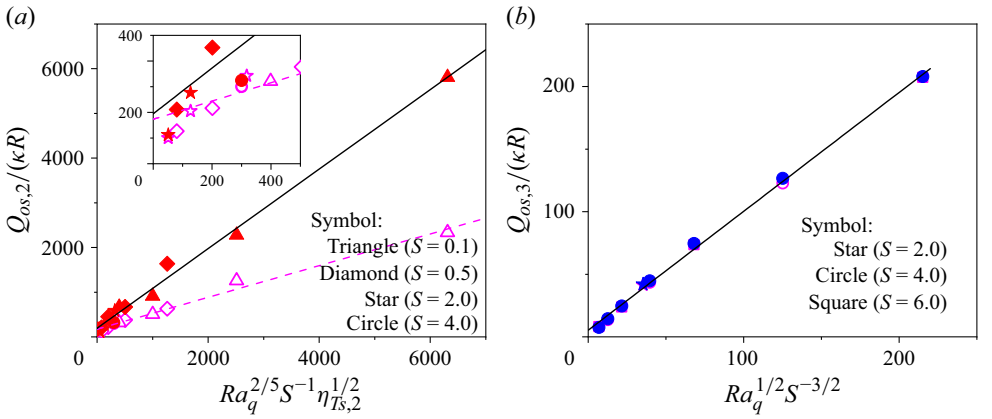


Figure 13. Flow rate in the pipe in the fully developed stage. The open and solid scatters are numerical results from cases of $D = 1.3$ and 4.0, respectively. (*a*) Cases in regime R2 with the solid line corresponding to the scaling law (3.31). (*b*) Cases in regime R3 with the solid line corresponding to the scaling law (3.41).

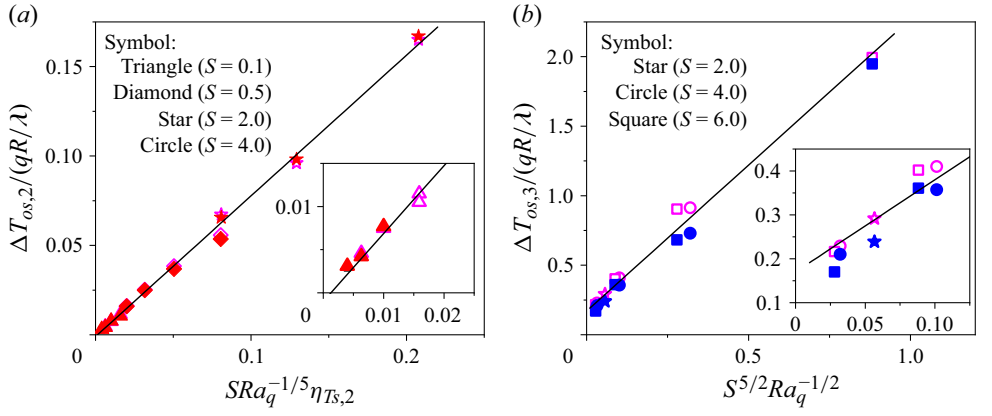


Figure 14. Validation of the temperature scales of flow at the outlet of the pipe in the fully developed stage. The open and solid scatters are numerical flow rates for cases in regimes R2 and R3, respectively. (*a*) Temperature scale for regime R2 (3.32). (*b*) Temperature scale for regime R3 (3.40).

are fitted by the relation

$$u_{vs,2}/(\kappa/R) = 0.62Ra_q^{2/5}S^{-1}\eta_{Ts,2}^{1/2} + 27.75, \tag{6.2}$$

as indicated by the solid line. As for regime R3, the numerical results in figure 12(*b*) also collapse onto the linear solid line, described by

$$u_{vs,3}/(\kappa/R) = 0.36Ra_q^{2/5}S^{-1}\eta_{Ts,2}^{1/2} + 6.67. \tag{6.3}$$

Figure 13(*a*) shows the numerical flow rate from the cases of $D = 1.3$ (open scatters) and $D = 4.0$ (solid scatters). The data for $D = 1.3$ and $D = 4.0$ fall on distinct linear relations. The dashed line and the solid line correspond to

$$Q_{os,2}/(\kappa R) = 0.36Ra_q^{2/5}S^{-1}\eta_{Ts,2}^{1/2} + 173 \tag{6.4}$$

and

$$Q_{os,2}/(\kappa R) = 0.89Ra_q^{2/5}S^{-1}\eta_{Ts,2}^{1/2} + 19, \tag{6.5}$$

https://doi.org/10.1017/jfm.2026.11695 Published online by Cambridge University Press

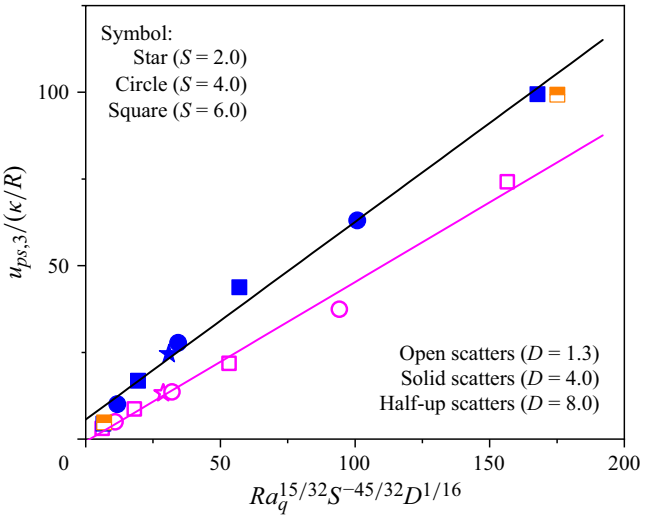


Figure 15. Validation of the velocity scale (4.14) of the thermal plume in the fully developed stage. The scatters are numerical results of cases in regime R3, and the maximal velocities at $z' = 0.5H$ are used.

respectively. For the same $Ra_q^{2/5}S^{-1}\eta_{Ts,2}^{1/2}$, the flow rate for $D = 1.3$ is slightly lower than for $D = 4.0$. It suggests that the free surface introduces a resistance to the vertical motion of the flow. In all, the scale $Ra_q^{2/5}S^{-1}\eta_{Ts,2}^{1/2}$ effectively predicts the fully developed flow rate at the pipe outlet in regime R2.

In regime R3, when the thermal boundary layer merges, the numerical results for both $D = 1.3$ and $D = 4.0$ collapse onto a single solid line, as shown in figure 13(*b*). Consequently, the outlet flow rate in regime R3 follows a $Ra_q^{1/2}S^{3/2}$ scaling and becomes insensitive to D for $D > 1.3$. This is because the upward flow velocity and flow rate in regime R3 are lower than in regime R2, as can be observed by comparing figures 12 and 13.

Figure 14 compares the numerical outlet temperatures with the scaling laws, showing excellent agreement in both regimes R2 and R3. The data collapse onto lines with slopes and intercepts of (0.787, −0.001) for regime R2 and (2.061, 0.169) for regime R3, in panels (*a*) and (*b*) respectively. This close agreement confirms that the scales $SRa_q^{-1/5}\eta_{Ts,2}$ and $S^{5/2}Ra_q^{-1/2}$ accurately predict the outlet temperature for regimes R2 and R3, respectively.

6.2. *Thermal plume and intrusion flow*

Figure 15 presents the maximum upward velocity in the vertical profile of the thermal plume, obtained at a location midway between the outlet and the free surface (i.e. at $z' = 0.5H$). The numerical results for $D = 4.0$ collapse onto the solid line defined by

$$u_{ps,3}/(\kappa/R) = 0.57Ra_q^{15/32}S^{-45/32}D^{1/16} + 5.64. \tag{6.6}$$

In contrast, the data for $D = 1.3$ follow a separate, lower trend described by

$$u_{ps,3}/(\kappa/R) = 0.46Ra_q^{15/32}S^{-45/32}D^{1/16} - 0.72. \tag{6.7}$$

This indicates that for the same value of the scale $Ra_q^{15/32}S^{-45/32}D^{1/16}$, the plume velocity for $D = 1.3$ is lower than that for $D = 4.0$. This is because a smaller D brings the free surface closer, which impedes the vertical flow by constraining fluid motion and modifying

https://doi.org/10.1017/jfm.2026.11695 Published online by Cambridge University Press

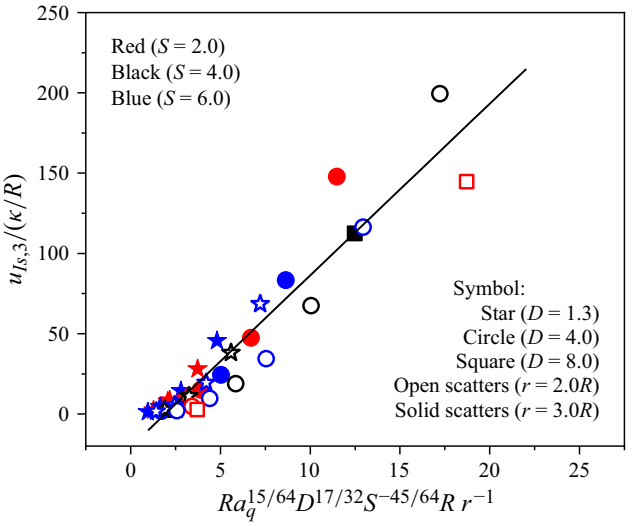


Figure 16. Validation of the velocity scale (5.9) of the spreading flow. The scatters are the maximal numerical velocity of cases in regime R3.

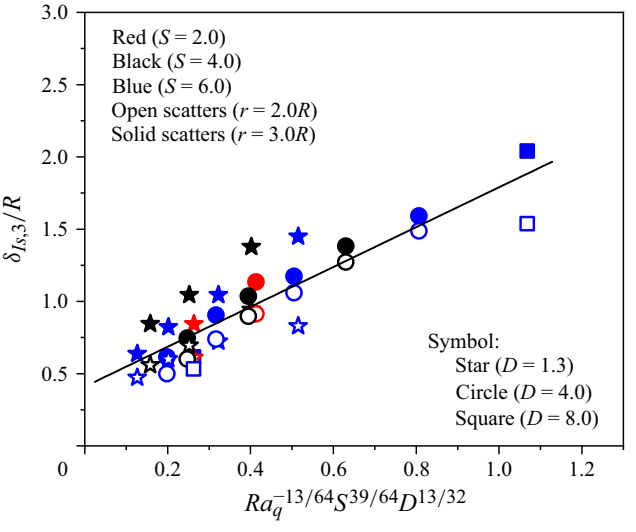


Figure 17. Validation of the thickness scale (5.10) of the spreading flow. The scatters are the numerical thickness of cases in regime R3.

the local pressure distribution. Compared with the significant change between $D = 1.3$ and $D = 4.0$, the difference between the data for $D = 4.0$ and $D = 8.0$ is marginal. This trend suggests that further increases in D no longer significantly affect the measured maximum velocity, and the plume at the measurement location gradually approaches a state where the influence of the pipe exit and upper boundary becomes negligible.

The velocity and thickness of the spreading flow were monitored at two streamwise locations, $r = 2.0R$ and $r = 3.0R$, and are compared with the scales in (5.9) and (5.10), respectively. The comparisons are presented in figure 16 for velocity and figure 17 for thickness.

https://doi.org/10.1017/jfm.2026.11695 Published online by Cambridge University Press

Figure 16 shows that the scaling law tends to underestimate the velocity at $r = 3.0R$ but overestimate it at $r = 2.0R$. A similar deviation is observed for the flow thickness in figure 17. This discrepancy arises because the scaling analysis assumes a balance between buoyancy and viscosity. However, at $r = 2.0R$, which is closer to the impinging region, inertial forces still play a certain driving role, resulting in a higher velocity and a thicker boundary layer due to more intense mixing than predicted. Furthermore, as shown in figure 17, the scaling law predicts the data for $D = 4$ and $D = 8$ better than for $D = 1.3$. This is consistent with the notion that the closer proximity to the free surface at smaller D introduces more significant mixing.

Despite these local discrepancies, the overall trends of the spreading flow are well captured by the scaling law. Based on the numerical data, the velocity and thickness can be estimated by

$$u_{Is,3}/(\kappa/R) = 10.69 Ra_q^{15/64} D^{17/32} S^{-45/64}(R/r) - 20.57,\ R^2_{adj} = 0.90 \tag{6.8}$$

and

$$\delta_{Is,3}/R = 1.38 Ra_q^{-13/64} S^{39/64} D^{13/32} + 0.41,\ R^2_{adj} = 0.79, \tag{6.9}$$

respectively. Here, R^2_{adj} is the adjusted R-squared value. The R^2_{adj} of the scaling law for spreading flow is lower than that for the pipe and plume flows. This is due to the accumulation of errors caused by the sequential assumptions in the scaling analysis from the pipe to the plume and finally to the spreading flow.

7. Conclusion

The buoyancy-driven flow system generated by submerged thermal vertical pipes comprises three key components: natural convection inside the pipe, a thermal plume above the pipe exit and a radial intrusion flow along the upper free surface. The system is governed by the Rayleigh number (Ra_q), slenderness ratio of the pipe (S) and the dimensionless submerged depth (D).

The axisymmetric natural convection in a pipe may evolve through three distinct routes: (i) the boundary layer flow, (ii) bulk momentum with a thermal boundary layer, and (iii) the pipe flow, depending on whether the velocity and thermal boundary layers merge at the pipe centre. These routes can be quantitatively distinguished by the dimensionless parameter $Ra_q S^{-5}$. Each route can be further divided into an unsteady stage and a fully developed stage, leading to the identification of complex flow regimes, as illustrated in figure 3. The fully developed dimensionless flow rates for the three routes follow the scaling laws $Ra_q^{1/5}\eta_{Ts,1}^{1/2}\eta_{vs,1}$, $Ra_q^{2/5}S^{-1}\eta_{Ts,2}^{1/2}$ and $Ra_q^{1/2}S^{-3/2}$, respectively. The characteristic dimensionless temperature scales as $Ra_q^{-1/5}S\eta_{Ts,1}$, $Ra_q^{-1/5}S\eta_{Ts,2}$ and $S^{5/2}Ra_q^{-1/2}$, respectively. The η parameters ($\eta_{Ts,1}$, $\eta_{vs,1}$, $\eta_{Ts,2}$) are functions of $Ra_q^{-1/5}S$ accounting for curvature effects. Scaling relations for the external thermal plume and radial intrusion flow resulting from the pipe flow regime are also established. The characteristic dimensionless velocity of the thermal plume scales as $D^{1/16}Ra_q^{15/32}S^{-45/32}$. For the radial intrusion, the local dimensionless velocity at a radial distance r scales as $D^{17/32}Ra_q^{15/64}S^{-45/64}(R/r)$, where R is the pipe radius. The proposed scaling laws show excellent agreement with numerical simulations within the investigated parameter ranges ($1.0^4 \leqslant Ra_q \leqslant 1.0^7$, $1.3 \leqslant D \leqslant 8.0$, $0.1 \leqslant S \leqslant 6.0$), in which the heat transfer and flow is axisymmetric and laminar.

https://doi.org/10.1017/jfm.2026.11695 Published online by Cambridge University Press

The ocean's vertical stratification creates a fundamental resource mismatch: a nutrient-poor sunlit layer overlies a light-deficient, nutrient-rich depth, limiting the biological carbon pump's efficiency (Wang *et al.* 2023) and influencing global climate. Artificial upwelling via vertical pipes in offshore oligotrophic waters can enhance vertical mass transport and alleviate this mismatch (Lovelock & Rapley 2007). One class of such systems is inspired by the perpetual salt fountain (Stommel, Arons & Blanchard 1956; Maruyama *et al.* 2011), where density differences sustained by temperature and salinity gradients drive sustained upward flow inside pipes. This mechanism avoids the rapid sinking of upwelled cold water that can occur in mechanically driven systems; however, it requires an initiation procedure and is highly dependent on specific oceanic temperature and salinity profiles. A potential variant involves using offshore solar energy to heat the pipe walls. The transient scaling analysis developed in this study provides a framework for understanding flow development under such time-dependent thermal forcing. Future work should validate these scaling relations over a broader parameter space, particularly for large slenderness ratios and Rayleigh numbers where oceanic artificial upwelling applications would operate.

Acknowledgements. We are thankful for the technical support of the National Large Scientific and Technological Infrastructure 'Earth System Numerical Simulation Facility' (https://cstr.cn/31134.02.EL).

Funding. The study is financially supported by the National Natural Science Foundation of China (Grant No. 12372381).

Declaration of interests. The authors claim no conflict of interest.

Data availability statement. Any data generated or analysed during this study can be obtained from the corresponding author upon reasonable request.

Appendix A. Numerical set-up

The governing equations (2.1)–(2.4) were solved using the finite-volume method with the SIMPLE (semi-implicit method for pressure-linked equations) scheme. The linear second derivatives and first derivatives were approximated by a second-order centre-differencing scheme. The nonlinear advection terms were discretised using a QUICK (quadratic upwind interpolation for convective kinetics) scheme. Time integration was performed by using the implicit second-order scheme. The solver has been validated for natural convection adjacent to walls in our previous studies (Ma *et al.* 2018*b*; Nie & Xu 2022; Jiang *et al.* 2024).

The computational domain is an axisymmetric two-dimensional region, with the axis of symmetry coinciding with the central axis of the circular pipe, as shown in figure 18. The no-slip boundary condition (2.7) and the isoflux condition (2.8) were applied to the pipe wall. The Bernoulli boundary condition for pressure and the zero-gradient velocity condition were adopted at the lower inlet boundary of the pipe (also see Kogawa *et al.* 2016), while the zero-gradient conditions for both pressure and velocity were applied at the remaining open boundaries. The temperature of the backflow remained constant at T_0. The direction of the backflow was aligned with that of the adjacent interior cell.

Independence studies for the grid, computational domain size and time step were conducted for the case with $S = 6.0$, $Ra_q = 10^7$ and $D = 1.3$, which exhibits a strong intrusion flow. After testing r_{max} from $3R$ to $9R$, the computational domain was determined to satisfy $r_{max} \geqslant 5R$. Additionally, the open boundary aligned with the free surface was positioned at $z' \geqslant H + 2R$ to minimise its effects on plume entrainment at the pipe exit. A non-uniform structured grid was employed, with local refinement near the pipe wall, pipe inlet, pipe outlet and the free surface to resolve the intense local spatial variations in flow and heat transfer. The total number of grids in each case

https://doi.org/10.1017/jfm.2026.11695 Published online by Cambridge University Press

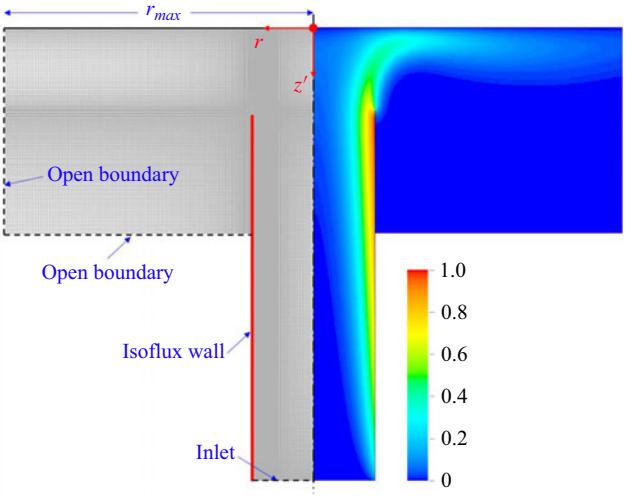


Figure 18. Numerical set-up for case $S = 6.0$, $Ra_q = 10^7$, $D = 1.33$. Left half: computational grids. Right half: fully developed temperature field $\Delta T/\Delta T_{max}$.

exceeded 299 000. Adaptive time stepping was used with a Courant number less than 0.8. Furthermore, an upper bound was imposed on the time step based on independence tests from previous studies (Ma *et al.* 2018*b*). The maximum non-dimensional time step was set to $0.016(\Delta t/(L^2/(\kappa Ra_q^{2/5}))$. The same strategy for the design of domain size, mesh and time steps was employed in all other cases.

References

Al-Arabi, M., Khamis, M. & Abd-Ul-Aziz, M. 1991 Heat transfer by natural convection from the inside surface of a uniformly heated tube at different angles of inclination. *Intl J. Heat Mass Transfer* **34** (4–5), 1019–1025.

Bae, J.-W., Kim, W.-K. & Chung, B.-J. 2018 Visualization of natural convection heat transfer inside an inclined circular pipe. *Intl Commun. Heat Mass Transfer* **92**, 15–22.

Batchelor, G.K. 1954 Heat convection and buoyancy effects in fluids. *Q. J. R. Meteorol. Soc.* **80** (345), 339–358.

Bonnecaze, R.T., Huppert, H.E. & Lister, J.R. 1993 Particle-driven gravity currents. *J. Fluid Mech.* **250**, 339–369.

Brand, R.S. & Lahey, F.J. 1967 The heated laminar vertical jet. *J. Fluid Mech.* **29** (2), 305–315.

Cebeci, T., Wogulis, E.R. & Partin, R.D. 1968 Effect of transverse curvature on skin friction and heat transfer in laminar flows past slender circular cylinders. *J. Heat Transfer* **90** (4), 485–487.

Dash, M.K. & Dash, S.K. 2020 Natural convection heat transfer and fluid flow around a thick hollow vertical cylinder suspended in air: a numerical approach. *Intl J. Therm. Sci.* **152**, 106312.

Davis, L.P. & Perona, J.J. 1971 Development of free convection flow of a gas in a heated vertical open tube. *Intl J. Heat Mass Transfer* **14** (7), 889–903.

Didden, N. & Maxworthy, T. 1982 The viscous spreading of plane and axisymmetric gravity currents. *J. Fluid Mech.* **121**, 27–42.

Dyer, J.R. 1975 The development of laminar natural-convective flow in a vertical uniform heat flux duct. *Intl J. Heat Mass Transfer* **18** (12), 1455–1465.

Gohil, T.B., Saha, A.K. & Muralidhar, K. 2012 Numerical study of instability mechanisms in a circular jet at low Reynolds numbers. *Comput. Fluids* **64**, 1–18.

Goodrich, S.S. & Marcum, W.R. 2019 Natural convection heat transfer and boundary layer transition for vertical heated cylinders. *Exp. Therm. Fluid Sci.* **105**, 367–380.

Hosseini, R., Rezania, A., Alipour, M. & Rosendahl, L.A. 2012 Natural convection heat transfer from a long heated vertical cylinder to an adjacent air gap of concentric and eccentric conditions. *Heat Mass Transfer* **48** (1), 55–60.

Hoult, D.P. 1972 Oil spreading on the sea. *Annu. Rev. Fluid Mech.* **4** (1), 341–368.

https://doi.org/10.1017/jfm.2026.11695 Published online by Cambridge University Press

HUANG, Y., GE, J., CHEN, Y. & ZHANG, C. 2023 Natural and forced convection heat transfer characteristics of single-phase immersion cooling systems for data centers. *Intl J. Heat Mass Transfer* **207**, 124023.

HUNT, G.R. & VAN DEN BREMER, T.S. 2011 Classical plume theory: 1937–2010 and beyond. *IMA J. Appl. Maths* **76** (3), 424–448.

HUPPERT, H.E. 1982 The propagation of two-dimensional and axisymmetric viscous gravity currents over a rigid horizontal surface. *J. Fluid Mech.* **121**, 43–58.

JAPIKSE, D. 1973 Advances in thermosyphon technology. In *Advances in Heat Transfer*, vol. 9, pp. 1–111. Elsevier.

JIANG, Y., NIE, B., ZHAO, Y., CARMELIET, J. & XU, F. 2021 Scaling of buoyancy-driven flows on a horizontal plate subject to a ramp heating of a finite time. *Intl J. Heat Mass Transfer* **171**, 121061.

JIANG, Y., ZHAO, Y., CARMELIET, J., NIE, B. & XU, F. 2024 Critical transitions on a route to chaos of natural convection on a heated horizontal circular surface. *J. Fluid Mech.* **988**, A38.

KAMINSKI, E. & JAUPART, C. 2003 Laminar starting plumes in high-Prandtl-number fluids. *J. Fluid Mech.* **478**, 287–298.

KOGAWA, T., OKAJIMA, J., KOMIYA, A., ARMFIELD, S.W. & MARUYAMA, S. 2016 Large eddy simulation of turbulent natural convection between symmetrically heated vertical parallel plates for water. *Intl J. Heat Mass Transfer* **101**, 870–877.

LIN, W. & ARMFIELD, S.W. 2001 Natural convection cooling of rectangular and cylindrical containers. *Intl J. Heat Fluid Flow* **22** (1), 72–81.

LIN, W. & ARMFIELD, S.W. 2012 Unified Prandtl number scaling for start-up and fully developed natural-convection boundary layers for both $Pr \gtrsim 1$ and $Pr \lesssim 1$ fluids with isothermal heating. *Phys. Rev. E* **86** (6), 066312.

LIN, W. & ARMFIELD, S.W. 2013 Scalings for unsteady natural convection boundary layers on an evenly heated plate with time-dependent heating flux. *Phys. Rev. E* **88** (6), 063013.

LIN, W., ARMFIELD, S.W., PATTERSON, J.C. & LEI, C. 2009 Prandtl number scaling of unsteady natural convection boundary layers for $Pr > 1$ fluids under isothermal heating. *Phys. Rev. E* **79** (6), 066313.

LIU, Y. & LIU, C. 2022 Unified scale laws for transient convective boundary layers: from flat to curved boundary layers. *Phys. Rev. Fluids* **7** (5), 054101.

LOVELOCK, J.E. & RAPLEY, C.G. 2007 Ocean pipes could help the Earth to cure itself. *Nature* **449** (7161), 403–403.

MA, J., NIE, B. & XU, F. 2018*a* $\mathrm{Pr} > 1$ unsteady thermal flows and heat transfer in a finned cavity with a uniform heat flux. *Intl J. Therm. Sci.* **129**, 83–93.

MA, J., NIE, B. & XU, F. 2018*b* Transient flows on an evenly heated wall with a fin. *Intl J. Heat Mass Transfer* **118**, 235–246.

MAO, Y., LEI, C. & PATTERSON, J.C. 2010 Unsteady near-shore natural convection induced by surface cooling. *J. Fluid Mech.* **642**, 213–233.

MARUYAMA, S., YABUKI, T., SATO, T., TSUBAKI, K., KOMIYA, A., WATANABE, M., KAWAMURA, H. & TSUKAMOTO, K. 2011 Evidences of increasing primary production in the ocean by Stommel's perpetual salt fountain. *Deep Sea Res. I: Oceanogr. Res. Papers* **58** (5), 567–574.

MOKHEIMER, E.M.A. & EL-SHAARAWI, M.A.I. 2007 Correlations for maximum possible induced flow rates and heat transfer parameters in open-ended vertical eccentric annuli. *Intl Commun. Heat Mass Transfer* **34** (3), 357–368.

MORTON, B.R., TAYLOR, G.I. & TURNER, J.S. 1956 Turbulent gravitational convection from maintained and instantaneous sources. *Proc. R. Soc. Lond. A Math. Phys. Sci.* **234** (1196), 1–23.

NIE, B. & XU, F. 2022 Effect of curvature on transient natural convection in a vertical circular pipe. *J. Fluid Mech.* **937**, A29.

OHK, S.-M. & CHUNG, B.-J. 2017 Natural convection heat transfer inside an open vertical pipe: influences of length, diameter and Prandtl number. *Intl J. Therm. Sci.* **115**, 54–64.

PATTERSON, J. & IMBERGER, J. 1980 Unsteady natural convection in a rectangular cavity. *J. Fluid Mech.* **100** (1), 65–86.

PÉCHEUX, J., LE QUÉRÉ, P. & ABCHA, F. 1994 Curvature effects on axisymmetric instability of conduction regime in a tall air-filled annulus. *Phys. Fluids* **6** (10), 3247–3255.

STOMMEL, H., ARONS, A.B. & BLANCHARD, D. 1956 An ocean curiosity: the perpetual salt fountain. *Deep Sea Res.* **3**, 152–153.

TAKHAR, H.S. 1968 Entry-length flow in a vertical cooled pipe. *J. Fluid Mech.* **34** (4), 641–650.

WANG, W.-L., FU, W., MOIGNE, L., FRÉDÉRIC, A.C., LETSCHER, R.T., LIU, Y., TANG, J.-M. & PRIMEAU, F.W. 2023 Biological carbon pump estimate based on multidecadal hydrographic data. *Nature* **624** (7992), 579–585.

https://doi.org/10.1017/jfm.2026.11695 Published online by Cambridge University Press

XU, F., PATTERSON, J.C. & LEI, C. 2009 Transient natural convection flows around a thin fin on the sidewall of a differentially heated cavity. *J. Fluid Mech.* **639**, 261–290.

YU, P., PATTERSON, J.C. & LEI, C. 2015 A scaling analysis of transient natural convection in a reservoir model induced by iso-flux heating. *J. Fluid Mech.* **764**, 219–249.

ZHANG, W., NIE, B. & XU, F. 2023 Experiment of a thermal plume on an open cylinder. *J. Fluid Mech.* **974**, A6.

ZHAO, Y., LEI, C. & PATTERSON, J.C. 2021 Magnified heat transfer from curved surfaces: a scaling prediction. *Phys. Fluids* **33**, 021702.

https://doi.org/10.1017/jfm.2026.11695 Published online by Cambridge University Press